

## Three Types of Indian Ocean Dipoles

FEIYAN GUO

*Physical Oceanography Laboratory/Qingdao Collaborative Innovation Center of Marine Science and Technology,  
Key Laboratory of Ocean–Atmosphere Interaction and Climate in Universities of Shandong, Ocean University of  
China, Qingdao, China, and NOAA/Earth System Research Laboratory, Boulder, Colorado*

QINYU LIU

*Physical Oceanography Laboratory/Qingdao Collaborative Innovation Center of Marine Science and Technology,  
Key Laboratory of Ocean–Atmosphere Interaction and Climate in Universities of Shandong, Ocean University of  
China, Qingdao, China*

S. SUN

*NOAA Earth System Research Laboratory, Boulder, Colorado*

JIANLING YANG

*Key Laboratory of Meteorological Disaster Preventing and Reducing in Ningxia, Ningxia Institute of  
Meteorological Science, Yinchuan, China, and NOAA/Earth System Research Laboratory, Boulder, Colorado*

(Manuscript received 16 July 2014, in final form 22 January 2015)

### ABSTRACT

Using observational data and phase 5 of the Coupled Model Intercomparison Project (CMIP5) model outputs [the preindustrial (PI) control run of the Community Climate System Model, version 4 (CCSM4) and historical simulations of 17 CMIP5 models], Indian Ocean dipoles (IODs) with a peak in fall are categorized into three types. The first type is closely related to the development phase of El Niño/La Niña. The second type evolves from the basinwide warming (cooling) in the tropical Indian Ocean (IO), usually occurring in the year following El Niño (La Niña). The third type is independent of El Niño and La Niña. The dominant trigger condition for the first (third) type of IOD is the anomalous Walker circulation (anomalous cross-equatorial flow); the anomalous zonal sea surface temperature (SST) gradient in the tropical IO is the trigger condition for the second type. The occurrence of anomalous ocean Rossby waves during the forming stage of IO basinwide mode and their effect on SST in the southwestern IO during winter and spring are critical for early development of the second type of IOD. Although most models simulate a stronger El Niño–Southern Oscillation and IOD compared to the observations, this does not influence the phase-locking and classification of the IOD peaking in the fall.

### 1. Introduction

In the tropical Indian Ocean (TIO), the Indian Ocean dipole (IOD) mode is one of the important ocean–atmosphere coupled natural modes (Saji et al. 1999; Webster et al. 1999) and has great influence on the

surrounding climate (Ashok et al. 2001; Black et al. 2003; Yamagata et al. 2004; Behera et al. 2005; Meyers et al. 2007; Cai et al. 2009a,b). Most IOD events start from sea surface temperature anomalies (SSTAs) near the Java coast in response to the surface wind anomalies (SWAs) (Saji et al. 1999; Saji and Yamagata 2003; Behera et al. 2006). The SWAs (anomalous strong southeasterly winds) may be caused by the anomalous Indian monsoon (Behera et al. 1999, 2006; Annamalai et al. 2003) during positive IOD events, or remote forcing from El Niño–Southern Oscillation (ENSO), which is the strongest natural interannual climate fluctuation (Philander 1990),

*Corresponding author address:* Qinyu Liu, Physical Oceanography Laboratory/Qingdao Collaborative Innovation Center of Marine Science and Technology, Ocean University of China, Qingdao, China, 266100.  
E-mail: liuqyou@gmail.com

influencing the entire global climate system (Rasmusson and Carpenter 1982; Bradley et al. 1987; Privalsky and Jensen 1995; Trenberth et al. 1998; Xie et al. 2010; Cai et al. 2012; Zhou et al. 2014). Finding the relationship between an IOD and ENSO has been a hot topic. Therefore, identifying the trigger conditions for IOD is crucial.

Earlier studies pointed out that the formation of the IOD is the result of local air-sea interaction in the TIO (Saji et al. 1999; Ashok et al. 2003; Yamagata et al. 2004). Some local air-sea interaction processes in the TIO during the developing stage include the zonal wind-thermocline-sea surface temperature (SST) feedback process (Saji et al. 1999), the wind-evaporation-SST (WES) feedback (Xie and Philander 1994; Li et al. 2003), the oceanic Rossby wave adjustive process (Webster et al. 1999; Xie et al. 2002; Huang and Kinter 2002; Rao and Behera 2005; Spencer et al. 2005), coastal upwelling (Vinayachandran et al. 1999; Murtugudde et al. 2000), evaporative cooling (Behera et al. 1999; Shinoda et al. 2004a), and the SST-cloud-radiation (SCR) feedback (Hong et al. 2008a,b), as mostly reviewed in Cai et al. (2013), which eventually lead to the occurrence of an IOD. Rao et al. (2002) and Rao and Behera (2005) pointed out that the downwelling equatorial Kelvin waves, reflected at Somali coast from the westward propagating equatorial Rossby waves, favor terminating a positive IOD and exciting a negative IOD. Guo et al. (2013) also found that the barrier layer in the southeastern Arabian Sea plays an important role during the development of positive IOD events. Many studies considered the IOD to be independent of ENSO (Saji et al. 1999; Anderson 1999; Ashok et al. 2003; Yamagata et al. 2003, 2004), such as the 1961 IOD event, without any large SSTAs in the tropical Pacific (TP).

Although the idea of a local origin of the IOD was widely accepted at one time, recent studies have found that ENSO can strongly condition the initiation and evolution of the IOD (Allan et al. 2001; Bracco et al. 2005; Behera et al. 2006; Saji et al. 2006; Cai et al. 2011, 2012; Hong et al. 2014), such as the 1997 IOD event. Izumo et al. (2010) demonstrated that IOD events tend not only to co-occur with ENSO events, but also to lead them. The ENSO and IOD are linked (Shinoda et al. 2004b; Zheng et al. 2010) and can lead to each other through tropospheric biennial oscillation (TBO; Meehl et al. 2003; Loschnigg et al. 2003). Thus, the focal point of argument about the relationship of the IOD and ENSO, is what triggers the IOD.

Previous studies have discussed the trigger condition of the IOD during the developing phase of ENSO (Yu and Rienecker 2000; Annamalai et al. 2003; Gualdi et al. 2003; Fischer et al. 2005; Zhong et al. 2005; Hong et al. 2010). As an El Niño develops in the equatorial Pacific, easterly anomalies induced by weakened Walker

circulation (WC) over the Indo-Pacific region develop along the equator in the Indian Ocean (IO), and the wind-thermocline-SST feedback eventually leads to the occurrence of an IOD. Beyond that, whether there is any IOD event in the year after an ENSO is unclear. Following an El Niño (La Niña) mature phase, an IO basinwide warming (cooling) usually takes place over the TIO (Klein et al. 1999; Lau and Nath 2003; Chowdary and Gnanaseelan 2007; Schott et al. 2009; Yang et al. 2010; Liu et al. 2013). As the basinwide warming develops, the inhomogeneous warming with anomalous zonal SST gradient in the TIO will also lead to SWAs over the eastern IO, and then trigger the IOD. Thus we propose this as another trigger condition for IOD. In addition, the SWAs in the equatorial and eastern IO induced by the interannual variability of cross-equatorial flow, such as the Asian monsoon (Fischer et al. 2005; Drbohlav et al. 2007; Terray et al. 2007) in the TIO, can directly influence upwelling along the coast of the Sumatra/Java islands, which can also be a trigger condition for the formation of an IOD.

Based on these analyses, we would like to address the following scientific questions: What are the trigger conditions for various IODs? Is their evolving process the same? What roles do ENSO and IO basinwide warming or cooling play in the different stage of an IOD? We will evaluate IODs based on model simulations combined with observations. Identifying different types of IODs with respective trigger conditions helps us further understand IOD characteristics. Besides, it is important to assess the similarities and differences in the evolution of different IODs.

The rest of this paper is organized as follows. Section 2 briefly describes the data source and methods. Sections 3, 4, and 5 mainly discuss the three types of IODs in observations and model simulations. Section 6 presents the conclusions and discussion.

## 2. Data and method

The Extended Reconstructed Sea Surface Temperature version 3b (ERSST.v3b) is used in this study to form indices and examine the associated anomalies from 1951 to 2013. The dataset is based on the International Comprehensive Ocean-Atmosphere Dataset (ICOADS) release 2.4, where local and short-term variations have been smoothed in ERSST (Smith et al. 2008). Associated variations in atmospheric circulation fields (surface wind) are obtained from the National Centers for Environmental Prediction (NCEP) reanalysis (Kalnay et al. 1996). Sea surface height (SSH) data are from the Simple Ocean Data Assimilation (SODA), version 2.2.4 (Carton and Giese 2008).

TABLE 1. List of the 17 CMIP5 models for historical simulations. Expansions of acronyms are available online at <http://www.ametsoc.org/PubsAcronymList>.

Identifier	CMIP5 model name	Short name of the institute	Country
(a)	CanESM2	CCCMA	Canada
(b)	CCSM4	NCAR	United States
(c)	CNRM-CM5	CNRM-CERFACS	Europe
(d)	CSIRO-Mk3-6-0	CSIRO/QCCCE	Australia
(e)	GFDL-ESM2G	GFDL	United States
(f)	GFDL-ESM2M	GFDL	United States
(g)	GISS-E2-H	GISS	United States
(h)	GISS-E2-R	GISS	United States
(i)	HadGEM2-ES	MOHC	United Kingdom
(j)	INM-CM4	INM	Russia
(k)	IPSL-CM5A-LR	IPSL	France
(l)	IPSL-CM5A-MR	IPSL	France
(m)	MIROC5	MIROC	Japan
(n)	MPI-ESM-LR	MPI-M	Germany
(o)	MRI-CGCM3	MRI	Japan
(p)	NorESM1-M	NCC	Norway
(q)	NorESM1-ME	NCC	Norway

In this study we also adopted the climate model outputs from the World Climate Research Program (WCRP) phase 5 of the Coupled Model Intercomparison Project (CMIP5), organized by the Program for Climate Model Diagnosis and Intercomparison (PCMDI) for the Intergovernmental Panel on Climate Change (IPCC) Fifth Assessment Report (AR5). We choose 17 CMIP5 models, which are labeled with a letter from “a” to “q” in Table 1. Variables from both the oceanic and atmospheric components are downloaded from the CMIP5 multi-model data archive (<http://pcmdi9.llnl.gov>), including SST, SSH, zonal and meridional surface winds, and vertical wind velocity. SSH is used to represent the thermocline here, since SSH is shown to represent the tendency of interannual thermocline variation (Yu 2003).

In this study we analyze two sets of simulations: a 500-yr (from years 801 to 1300) preindustrial (PI) control run of the Community Climate System Model, version 4 (CCSM4) model (Deser et al. 2012) and the last 55-yr (from 1951 to 2005) historical simulation of 17 CMIP5 models (Taylor et al. 2012). Only one ensemble member (r1i1p1) from each CMIP5 model is used in the multi-model composition in order to ensure equal weighting from each model. The “historical” forcing runs are used to represent the present state. The spatial resolution varies among models and within the same model for oceanic and atmospheric variables. To facilitate comparisons between models, all oceanic variables are interpolated to a common longitude–latitude grid of  $1^\circ \times 1^\circ$  latitude–longitude resolution, and all atmospheric variables on a  $2^\circ \times 2.5^\circ$  latitude–longitude grid.

Model simulation skills are examined by performing an empirical orthogonal function (EOF) analysis of

SSTAs over the TP ( $20^\circ\text{S}$ – $20^\circ\text{N}$ ,  $120^\circ\text{E}$ – $80^\circ\text{W}$ ) and TIO ( $20^\circ\text{S}$ – $20^\circ\text{N}$ ,  $40^\circ$ – $110^\circ\text{E}$ ) for each model and the observations (Figs. 1 and 2). Although there are systematic biases in the westward extent of the maximum SSTAs in the model outputs, almost all models realistically simulate the location of maximum positive SST signal in the eastern Pacific except the CSIRO-Mk3.6.0 model, in which the maximum signal locates in the western Pacific. The INM-CM4 model simulates very weak ENSO amplitude (Fig. 1). The modeled spatial pattern of the IOD mode (east–west dipole pattern) associated with maximum SSTA signal along the Java/Sumatra coast is comparable with observations, but the intensity of the IOD in most models is stronger than in the observations due to the climate background wind biases (Li et al. 2015). The east pole of the IOD in GFDL-ESM2G and GISS-E2-R is located south of  $10^\circ\text{S}$  instead of in the equatorial eastern IO region, indicating biases in simulating the upwelling in these models. Although most model simulations of ENSO and IOD events are too strong, the models simulate the phase-locking reasonably well for ENSO (November–January) and the IOD (August–November) (Fig. 3). Detailed evaluations of ENSO and the IOD in CMIP5 models are available in previous studies (e.g., Guilyardi et al. 2012; Kim and Yu 2012; Cai and Cowan 2013; Cai et al. 2013; Zheng et al. 2013; Liu et al. 2013; Du et al. 2013b; Taschetto et al. 2014; Rao and Ren 2014; Bellenger et al. 2014; Li and Xie 2014; Liu et al. 2014; Li et al. 2015).

Considering intermodel differences in the simulations of the maximum SSTAs in the 17 models (Fig. 1), we choose regional averaged SSTAs ( $5^\circ\text{S}$ – $5^\circ\text{N}$ ,  $172^\circ\text{E}$ – $120^\circ\text{W}$ ) as the ENSO index defined by Alexander et al. (2002). It covers a larger area than Niño-3.4 and extends

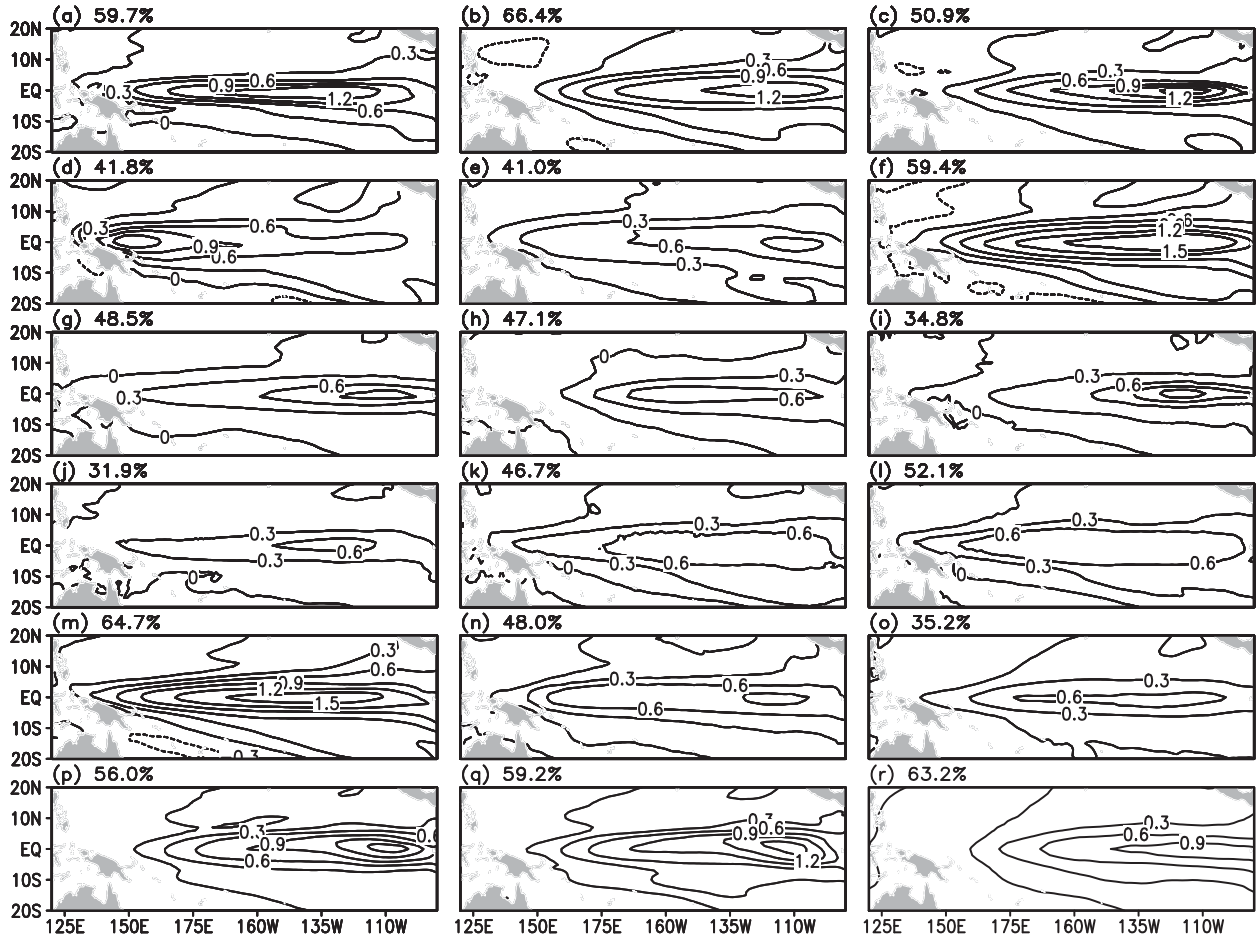


FIG. 1. Spatial patterns of the first EOF mode for the ENSO calculated from (a)–(q) 17 CMIP5 models and (r) ERSST observations. The values at the top of each panel are the explained variance.

farther westward, including the ENSO varying region in all the 17 models. As for the IOD events, we adopted the index defined by Saji et al. (1999): the difference of area mean SSTAs between the west pole of the IOD (IODW) region ( $10^{\circ}\text{S}$ – $10^{\circ}\text{N}$ ,  $50^{\circ}$ – $70^{\circ}\text{E}$ ) and the east pole of the IOD (IODE) region ( $10^{\circ}\text{S}$ – $0^{\circ}$ ,  $90^{\circ}$ – $110^{\circ}\text{E}$ ). For both observations and model simulations, an El Niño/La Niña event is identified if a 5-month running average of the ENSO index exceeds  $\pm 0.5$  standard deviations (STD) for at least three consecutive months; for a year to be considered as an IOD event, a 5-month running average of the SSTA should be greater than 0.8 STD with reverse signs in the IODW and IODE regions.

Since the IOD and ENSO are interannual variability modes, a 4- to 108-month band-passing filter is applied to extract the interannual signal for both the PI control run and the historical simulations. Composition analysis is adopted to study the trigger conditions and evolution processes of the IOD. A two-tailed Student's *t* test is conducted and only the results with statistical significance

at the 90% (95%) confidence level are shown in the spatial plots in the observations (model simulations).

### 3. IOD events in the past 63-yr observations

During the past 63 years, there are about 14 positive (pIOD; 1957, 1961, 1963, 1967, 1972, 1977, 1982, 1983, 1994, 1997, 2003, 2006, 2007, and 2012) and 14 negative (nIOD; 1954, 1958, 1960, 1964, 1974, 1975, 1981, 1984, 1989, 1996, 1998, 2001, 2005, and 2010) strong IOD events in all since 1951. Our results are consistent with the previous studies (Ashok et al. 2001 and 2003; Saji and Yamagata 2003; Yamagata et al. 2003; Behera et al. 2008; Guo et al. 2013; Fasullo and Boening et al. 2013; Du et al. 2013a). The most common pIOD (nIOD) events occurred during the developing phase of El Niño (La Niña) including 1957, 1963, 1972, 1982, 1994, 1997, and 2006 (1954, 1964, 1975, 1998, 2005, and 2010); besides, there are also some pIOD (nIOD) events appearing in the year following El Niño (La Niña) including 1977, 1983,

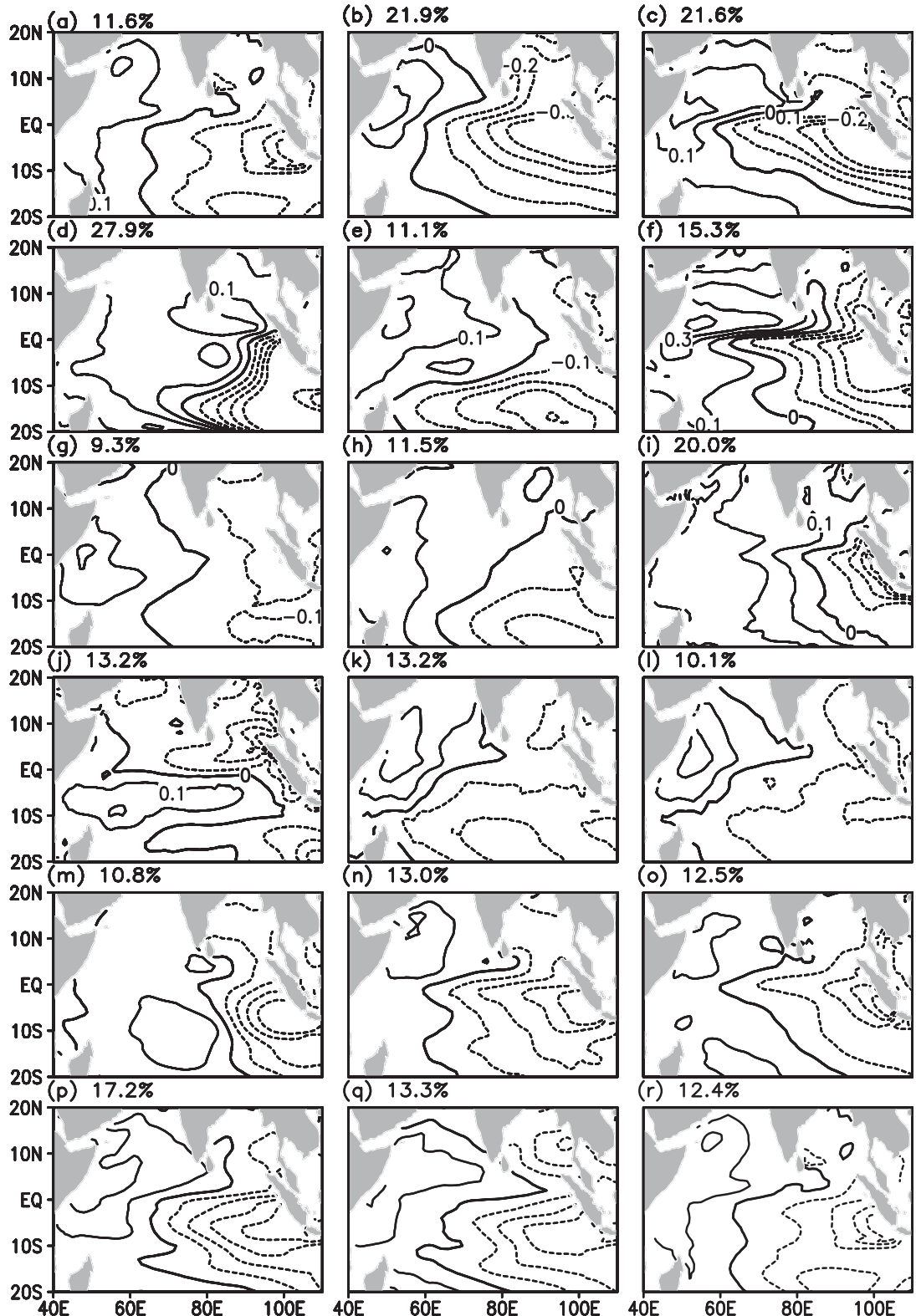


FIG. 2. Spatial patterns of the second (first mode for CSIRO-Mk3.6.0 and HadGEM2-ES) EOF mode for the IOD calculated from (a)–(q) 17 CMIP5 models and (r) ERSST observations. The values at the top of each panel are the explained variance.

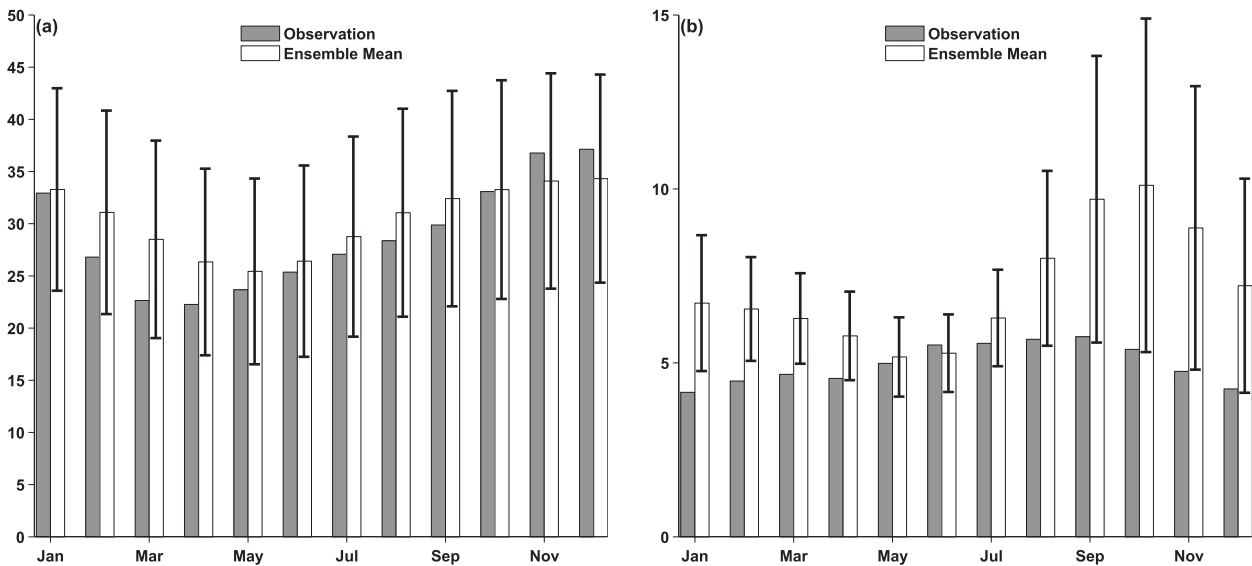


FIG. 3. Monthly standard deviations of the unnormalized PCs of the associated EOFs for the (a) TP and (b) TIO displayed in Figs. 1 and 2 from the observation (gray bar) and ensemble mean (white bar) of the 17 CMIP5 models. The error bars denote the standard deviation of intermodel variability.

2003, and 2007 (1974, 1981, 1984, 1989, 1996, and 2001). Some pIOD (nIOD) events even took place during the decaying phase of La Niña (El Niño) including 2012 (1958), and one positive IOD events occurred in 1967 during the developing phase of La Niña. In addition, some IODs happened without significant temperature anomalies in the TP, including 1960 and 1961, which are called pure IODs (Yamagata and Behera et al. 2004; Behera et al. 2006). Note that the year 1994 is debatable since this year has a strong pIOD and a weak El Niño signal (Saji and Yamagata 2003). Here we consider it as a common pIOD event that occurred during the developing phase of El Niño, following Du et al. (2013a).

According to the observational data above, there are some IODs that co-occur during the developing phase of El Niño (La Niña), and some pure IODs without the remote influence from TP. Little attention has been paid so far to the IODs occurring in the year after El Niño (La Niña), when the basinwide warming (cooling) in the TIO is known to follow the peak phase of El Niño (La Niña), which will undoubtedly result in regional changes in the TIO, such as atmospheric circulation (Yang et al. 2007; Du et al. 2013b). This new type of pIOD (nIOD) occurs in the year following El Niño (La Niña) and matures in

fall. This differs from the “unseasonable” IOD proposed by Du et al. (2013a), which is an intrinsic mode of the IO occurring without an ensuing El Niño (La Niña) and reaches its peak before summer. The three different categories of IODs are as follows (shown in Table 2): the first type are those pIODs (nIODs) occurring during the developing phase of El Niño (La Niña); the second type of IODs appear in the year following El Niño (La Niña); and the third type are pure IODs without any relation to ENSO. There are some consecutive IOD events (Behera et al. 2008) such as 2006 (first type) and 2007 (second type), and we put them into different types of IOD based on the classification criterion. We will focus on these three types of IODs in this paper. Their probabilities are 46.4%, 35.7%, and 7.1% of the total IOD for the three types respectively in the observations. There are very few special IOD events beyond the three categories described above, including pIOD (nIOD) events that occur during the first (second) year of La Niña (El Niño) (Behera et al. 2008) and IODs maturing before boreal summer with a short life cycle similar to the “unseasonable” IOD described in Du et al. (2013a). We will not address them in this work.

To capture some important features in the evolution of the three types of IODs, the bimonthly composite

TABLE 2. Classification of the three types of IODs for the observations.

Types	pIODs	nIODs
First type of IOD	1957, 1963, 1972, 1982, 1994, 1997, 2006	1954, 1964, 1975, 1998, 2005, 2010
Second type of IOD	1977, 1983, 2003, 2007	1974, 1981, 1984, 1989, 1996, 2001
Third type of IOD	1961	1960

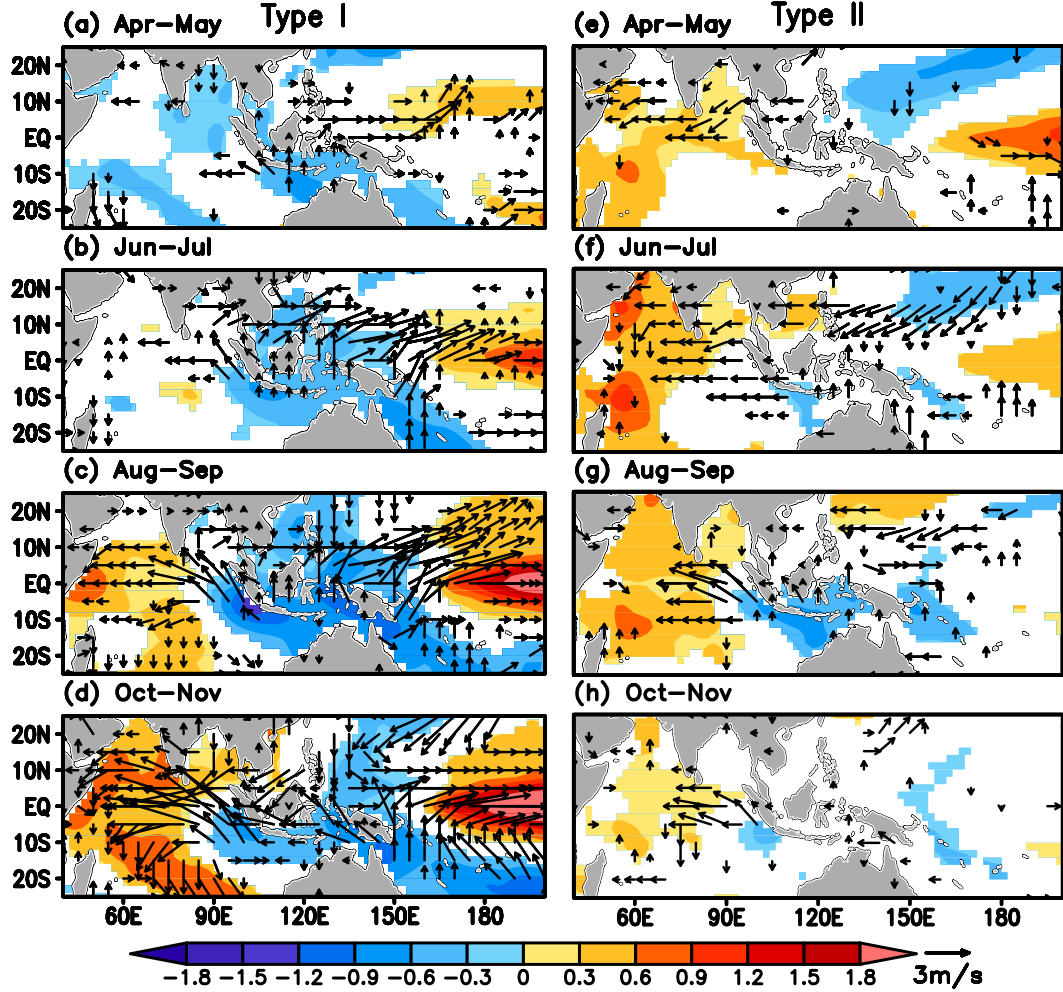


FIG. 4. Bimonthly mean differences (pIOD minus nIOD) of SSTAs (shaded,  $^{\circ}\text{C}$ ) and SWAs (vectors,  $\text{m s}^{-1}$ ) composite, for the (left) first and (right) second types of IOD. Shaded areas and vectors are of significant at the 90% confidence level, from a Student's two-tailed *t* test.

(positive phase minus negative phase) SSTAs, SSH anomalies (SSHAs) and SWAs during the whole life cycle (from April to November) for the first and second types of IODs are displayed in Figs. 4a–h and Figs. 5a–h, respectively. Only statistically significant results with a confidence level exceeding 90% are shown. As only one positive (1961) and one negative (1960) pure IOD event occurred since 1951, we analyzed the pure IOD that occurred in 1961 (Fig. 6).

#### a. The first type of IOD

There are 7 (6) pIODs (nIODs) of the first type since 1951 (shown in Table 2), which matures as El Niño (La Niña) develops in the TP. For the first type of positive IOD, the anomalous surface easterlies (Figs. 4a–d) due to the eastward shift of the Indo-Pacific WC (e.g., Rasmusson and Carpenter 1982) elevate the near-equatorial

thermocline (Figs. 5a–d) and increase anomalous evaporative cooling (Behera et al. 1999) in the east, which initially leads to cooling of the SST in the eastern IO (up to  $-1.2^{\circ}\text{C}$ ) by wind–thermocline–SST and WES feedbacks. Meanwhile, the remotely driven easterly anomalies also generate westward propagating downwelling Rossby waves (Figs. 5a–d), warming the SST ( $0.7^{\circ}\text{C}$ ) over the shallow thermocline “dome” region (e.g., Xie et al. 2002). Thus, the east–west dipole pattern forms in August–September and coevolves with variations in the TP, where a clear El Niño signal is depicted with a westward propagation of warm anomalies from the east to the west Pacific.

#### b. The second type of IOD

Four (six) pIODs (nIODs) of the second type occurred in the year following El Niño (La Niña) during

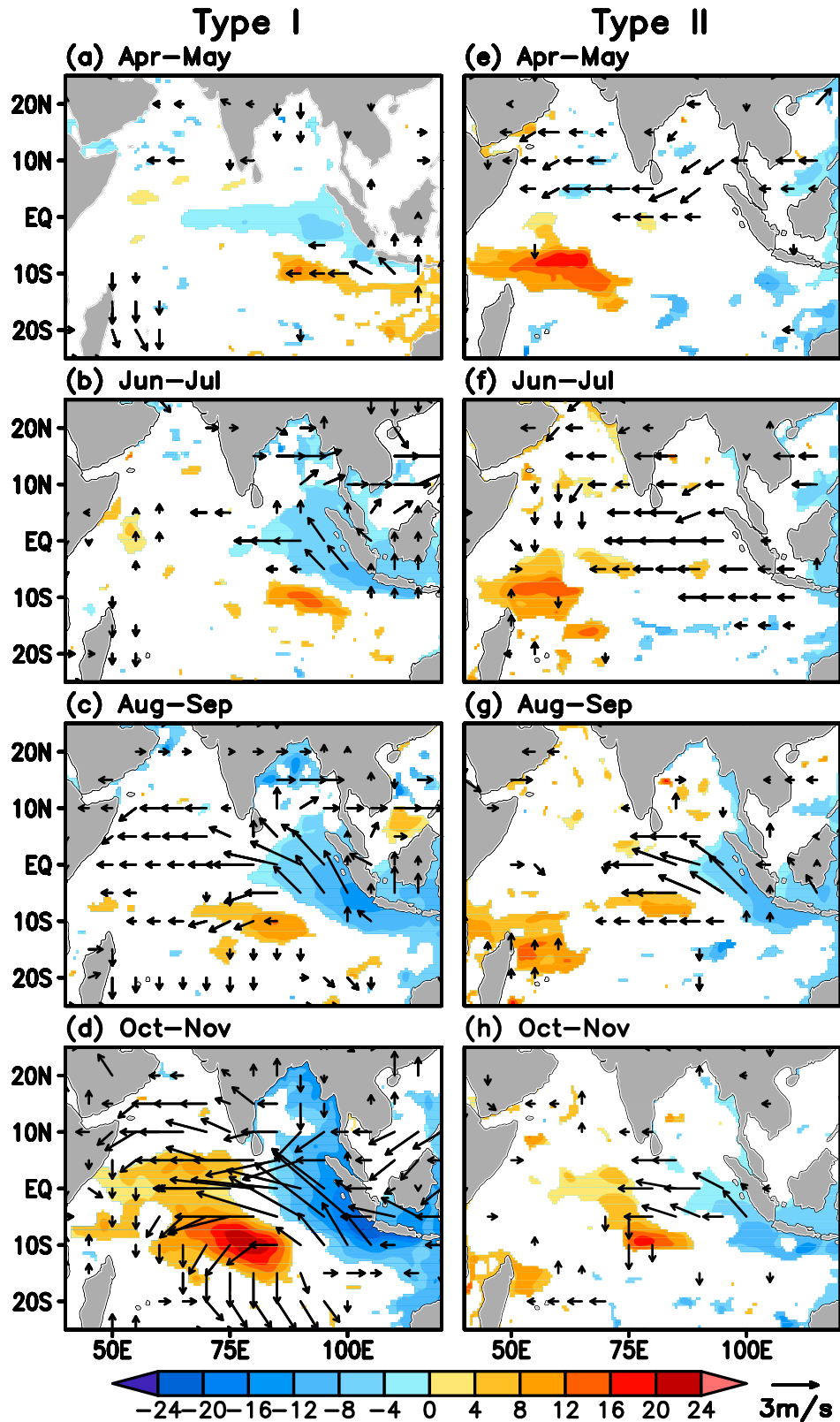


FIG. 5. As in Fig. 4, but for the SSHAs (color, cm) and SWAs (vectors,  $\text{m s}^{-1}$ ).

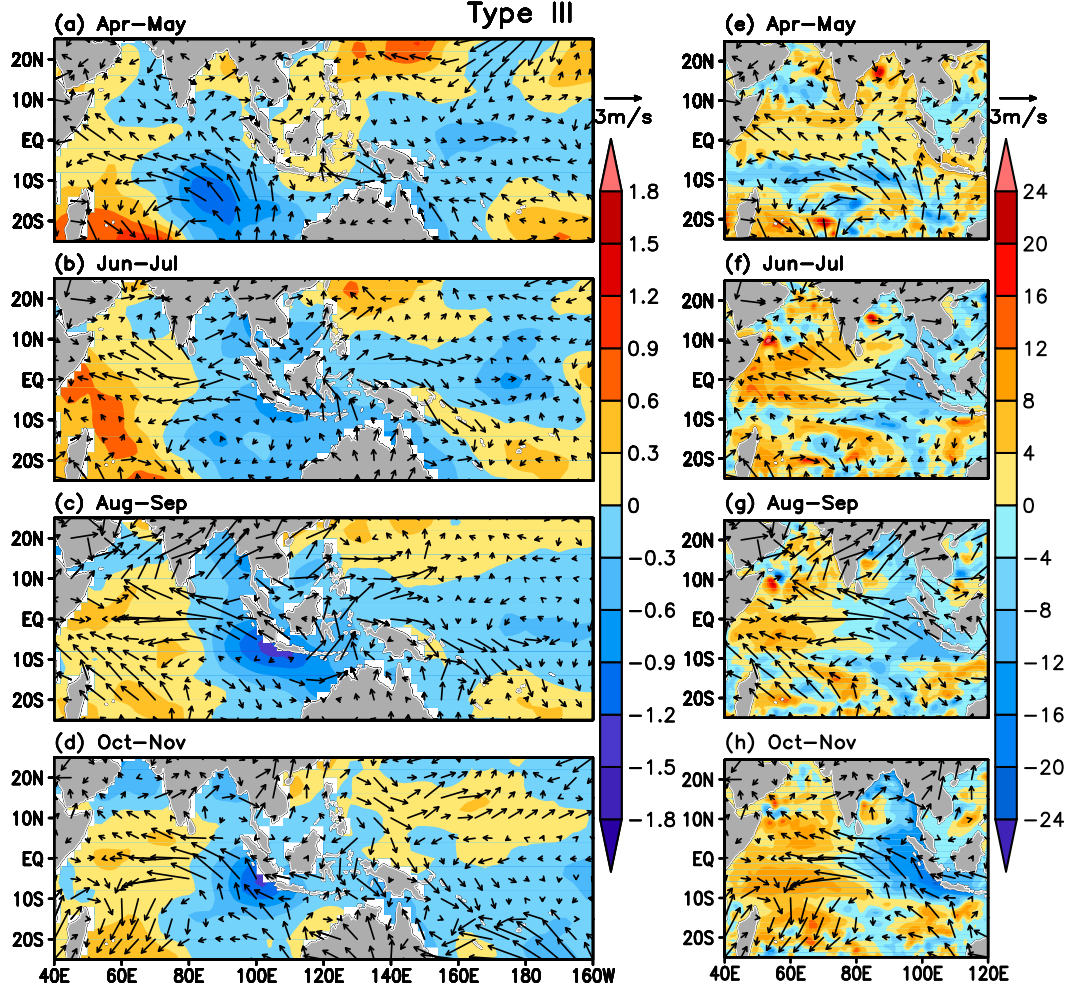


FIG. 6. Bimonthly mean of (left) SSTAs (shaded,  $^{\circ}\text{C}$ ) and SWAs (vectors,  $\text{m s}^{-1}$ ) and (right) SSHAs (shaded, cm) and SWAs (vectors,  $\text{m s}^{-1}$ ) for the third type of IOD that occurred in 1961.

the past 63 years (shown in Table 2). For the second type of pIOD (shown in Table 2) in boreal spring (April–May), the maximum positive SSTAs appear in the southwestern TIO dome region (Figs. 4e and 5e), which is likely to result from the downwelling Rossby wave induced by equatorial easterly anomaly in the TIO during last boreal fall and winter. Meanwhile, the anomalous easterlies prevail in the TIO (Figs. 4e,f), which are caused by the resulting zonal gradient in SSTAs (Fig. 4f). The SWAs partially offset the mean winds inducing SST warming (about  $0.6^{\circ}\text{C}$ ) in the northwestern TIO by a weakened evaporative cooling in June–July. Therefore the warm SSTAs can sustain in the west (Fig. 4f) and then intensify the zonal SST gradient. Furthermore, an anomalous zonal SST gradient promotes easterly anomalies in the equatorial and southeastern IO, which favors SST cooling in the eastern IO as a joint result of multiple mechanisms described in the

first type of IOD. Then an east–west dipole pattern occurs in August–September (Fig. 4g) and starts to decay in October–November (Fig. 4h). Unlike the first type of pIODs coevolving with El Niño, the formation of second type of pIODs develops in the second year of El Niño, which may be influenced more by an internal air-sea interaction within the TIO.

#### c. The third type of IOD

It seems that there is already a subtropical IOD in the case of the positive IOD (1961), and significant cross-equatorial southerly anomalies turn into southeasterly anomalies in the southeastern TIO in April–May (Fig. 6a), which promotes upwelling off the Sumatra/Java islands. Then the cold SSTAs extend eastward and northward, concentrated along the Sumatra/Java islands (Fig. 6b) with enhanced southeasterly anomalies, and the warm SSTAs gradually strengthen (about  $0.6^{\circ}\text{C}$ ) in

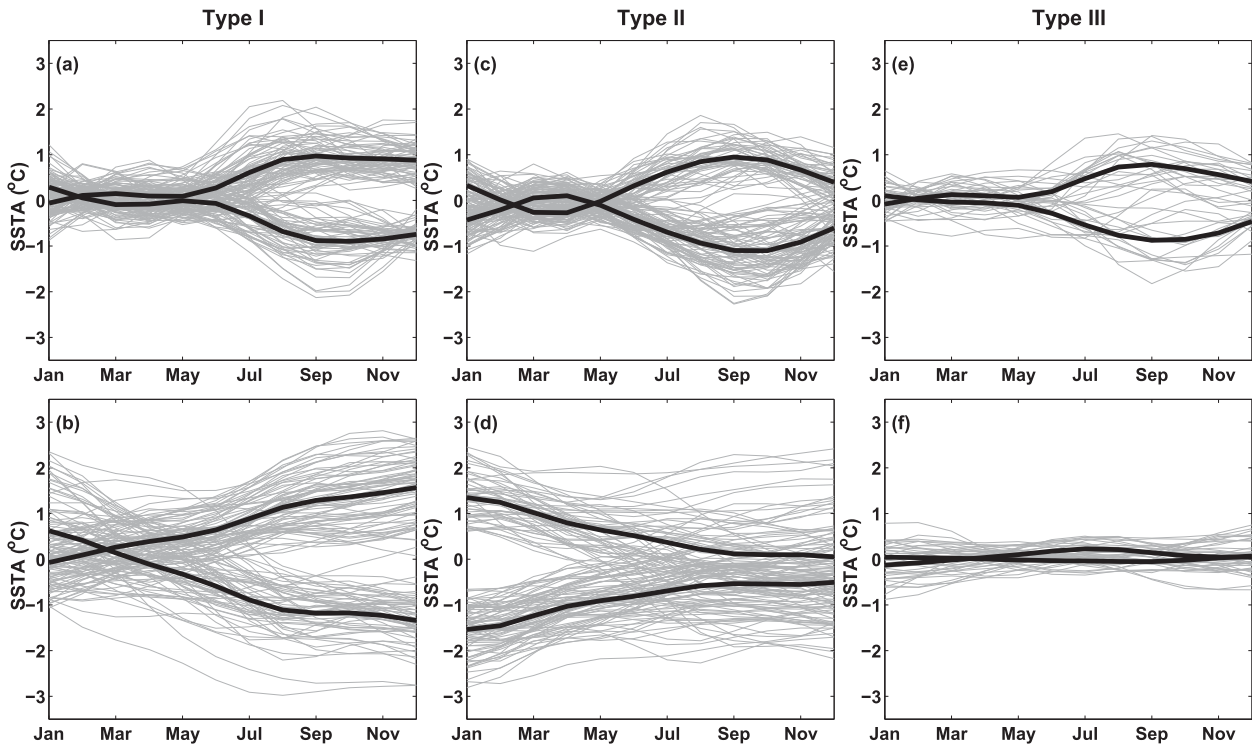


FIG. 7. Evolution of (a),(c),(e) the three types of IOD events (types I, II, and III, respectively) and (b),(d),(f) their corresponding ENSO indexes shown for the PI control run in CCSM4.

the western TIO caused by downwelling Rossby waves (Fig. 6f). Note that the pIOD that occurred in 1961 decays in October–November as do the first two types of IOD, but there are no obvious SSTAs across the TP during the development of the IOD.

Because of limited observations with only a few samples of each type of IOD events available, we now turn to general circulation models to take advantage of long model integrations in order to further investigate the three types of IODs with more samples. Next we will systematically investigate the three types of IOD events and assess different trigger conditions and their evolution processes using coupled model results.

#### 4. Three types of IODs in the PI control run of CCSM4

As we know, IOD is a natural interannual variability mode of the ocean–atmosphere interaction in the TIO, and its basic features should be captured in the PI control run without the greenhouse effect. We first investigate the IOD simulated in the PI control experiment in CCSM4. Only one model is employed first in order to avoid the complexity from multimodel simulations. We calculated the interannual variability of SST in the TIO and TP in the control experiment of CCSM4.

Using the 500-yr control run results, we find that there are 138 (147) El Niño (La Niña) and 154 (166) pIOD (nIOD) events, respectively. The IOD index for the three types and their corresponding ENSO index are shown in Fig. 7. Among these three types of IODs, there are 72 (58), 51 (79), and 22 (17) pIODs (nIODs), respectively, during the 500-yr control run of CCSM4. The third type is only 12.2%, far less than the first two types (both 40.6%), and is close to the observed probabilities of 7.1% in the past 63 years. As in the observations, there are only a few modeled consecutive IOD events belonging to both the first and second type of IOD. There are 14 special IOD events described in section 3 for the CCSM4 model, we do not discuss them in this study. Deser et al. (2012) pointed out that the CCSM4 simulates a very strong and periodic ENSO, which does not affect the classification results of the three types of IODs. With these model failures in mind, each of the three types of IODs does exist in the observations discussed in section 3, and the second type of IOD is not a model artifact due to an overly periodic and strong ENSO in the model outputs. Thus the model is still a useful tool when observations are limited in time or space.

To investigate the trigger condition and developing process, we first composite (positive phase minus negative phase) all variations during the whole life cycle

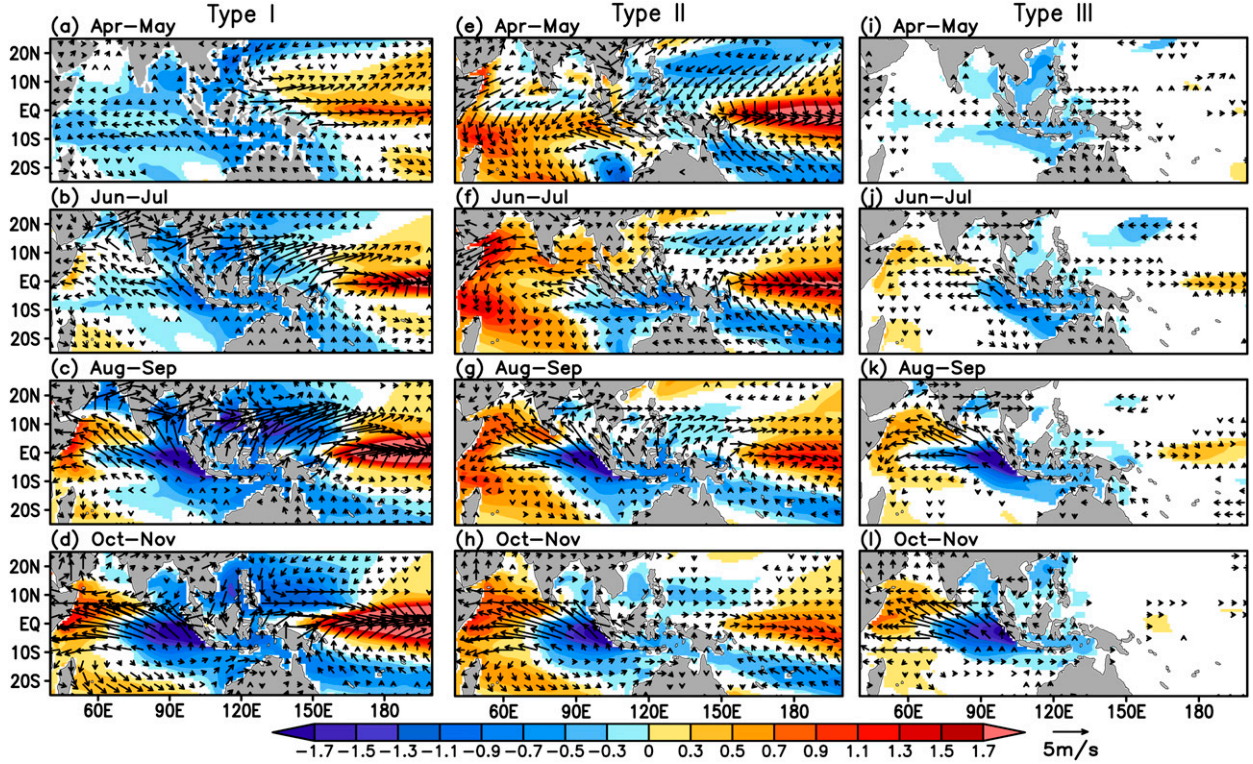


FIG. 8. Bimonthly differences (pIOD minus nIOD) of SSTA (shaded,  $^{\circ}\text{C}$ ) and SWA (vectors,  $\text{m s}^{-1}$ ) composites, for IOD types (left) I, (middle) II, and (right) III in the PI control run in CCSM4. Shaded areas and vectors are significant at the 95% confidence level, from a Student's two-tailed  $t$  test.

(from April to November) for the three types of IODs respectively in the control run as shown in Figs. 8, 9, and 10. Only statistically significant results with a confidence level exceeding 95% are shown.

#### a. Different trigger conditions for the three types of IODs

We find in Figs. 8 and 9 that the zonal wind anomalies in the equatorial and eastern IO appear before the formation of the dipole SST pattern for all the three types of IODs, but their trigger conditions are actually different from each other. For the first type of IOD, the easterly (westerly) anomalies are caused by the weakened (enhanced) Indo-Pacific WC (Fig. 9a), which results from the SSTAs in the TP when the El Niño (La Niña) develops there (Fig. 8a). This is consistent with previous studies mentioned earlier and the observational results. Unlike the first type, the WC in the third type has hardly any anomalies in the Pacific (Fig. 9i). It appears that in the absence of ENSO, the easterly (westerly) anomalies come from the strengthened (weakened) cross-equatorial flow such as the Asia–Australia summer monsoon with an easterly component in June–July (Fig. 8j), which is similar to the pure IOD in

the observations. Our results are in agreement with Fischer et al. (2005), who suggested that IOD events with no ENSO are triggered by an anomalous meridional Hadley cell accompanying an early northward penetration across the equator of the southeasterly trades in the eastern TIO.

As for the second type of IOD, an anomalous zonal SST gradient exist in the IO in the year following El Niño (La Niña), which triggers the easterly (westerly) anomalies in the equatorial and eastern IO as in the observations. Robust positive (negative) SSTAs (about  $1^{\circ}\text{C}$ ) appear in the thermocline dome area in the southwest IO (Fig. 8e), which are caused by the westward propagating downwelling (upwelling) oceanic Rossby waves in the IO (Fig. 10e) during the developing year of El Niño (La Niña). The cross-equatorial gradient in SSTAs in the western TIO triggers an asymmetric wind pattern (Wu et al. 2008; Du et al. 2009) with northeasterly (southwesterly) anomalies north and northwesterly (southeasterly) anomalies south of the equator, which is also seen in observations (Xie et al. 2002; Wu et al. 2008; Du et al. 2013b). The resulting asymmetric SWAs, cooling (warming) the SST in the northwestern TIO and warming (cooling) the SST in the southwestern

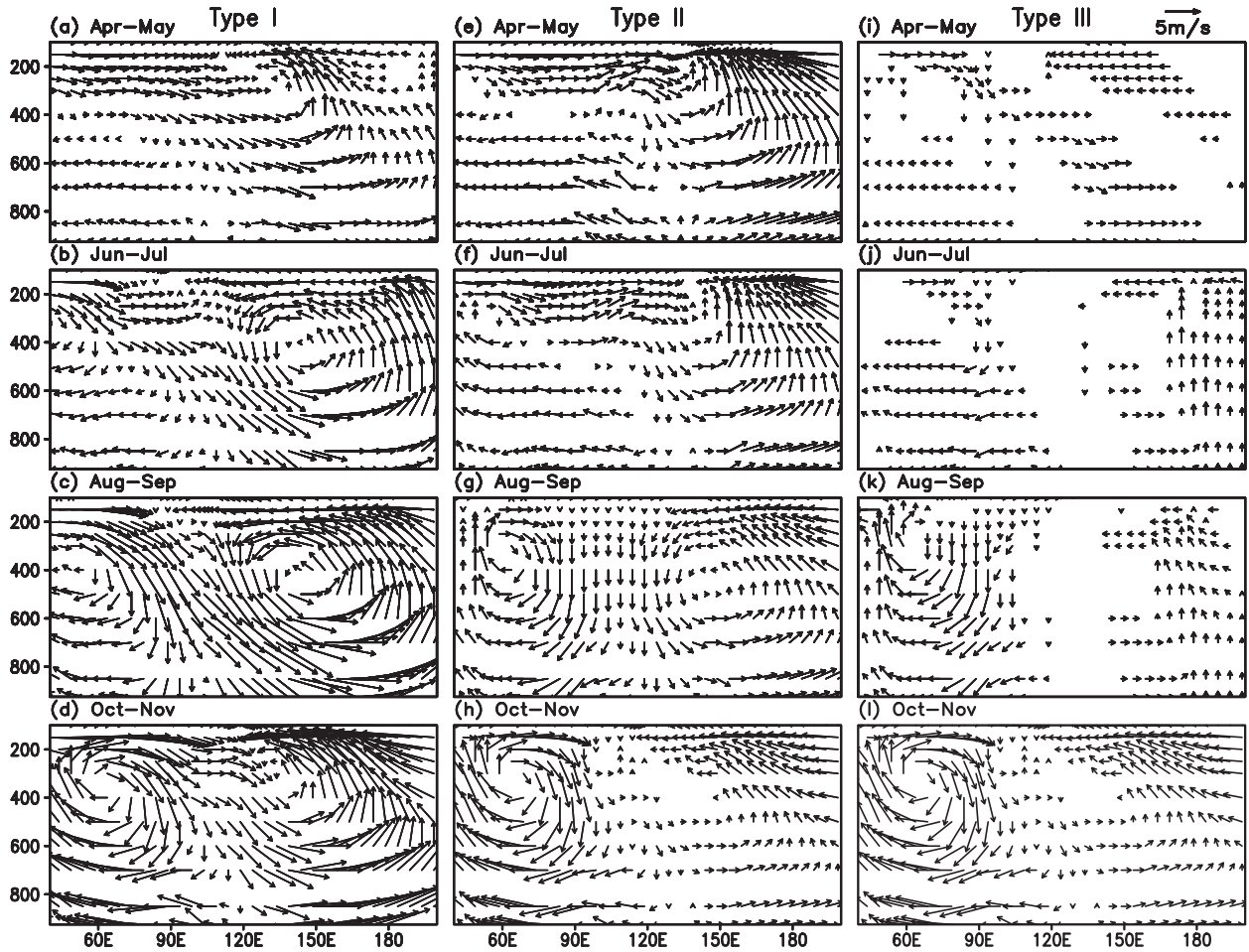


FIG. 9. Bimonthly composite anomaly (pIOD minus nIOD) of atmosphere circulation along the equator (meridian mean between 5°S and 5°N) for the three types of IOD in the PI control run in CCSM4. The zonal and vertical velocities are in  $\text{m s}^{-1}$  (vertical velocities units are  $\times 100$ ). All vectors are significant at the 95% confidence level, from a Student's two-tailed  $t$  test.

TIO by WES feedback, further amplify the inhomogeneous warming (cooling) cross the TIO in April–May (Fig. 8e). However, when the southwesterly monsoon onset occurs in boreal summer (Fig. 8f), the northeasterly (southwesterly) anomalies in the northwestern IO, in turn, counteract (superimpose on) the background winds, favoring local SST warming (cooling), up to  $\pm 1.3^\circ\text{C}$ , by reducing (increasing) evaporation in June–July (Fig. 8f). The second warming (cooling) over the northwestern IO has been detected in the observations and models (Du et al. 2009, 2013b). This persistent warming (cooling) over the western IO (maintaining over  $0.5^\circ\text{C}$ ) leads to an anomalous zonal SST gradient, which then causes easterly (westerly) anomalies converging (diverging) toward the western TIO. We conclude that the anomalous zonal SST gradient in the IO, resulting from the westward-propagating oceanic Rossby waves and WES feedback process in the year following El Niño (La Niña), is the

trigger condition for the second type of IOD. The Rossby waves affect SSTAs over thermocline dome region in the early stage of the IOD and are crucial for the formation of the second type.

#### b. Developing process of the three types of IODs

We find that the anomalous easterlies (westerlies) first appear in the equatorial and eastern IO in both the first and third types of IODs, which then induce anomalous cold (warm) SSTs in the eastern pole of the IO by the wind–thermocline–SST feedback process. Unlike the first and third types of IODs, it is the significant positive (negative) SSTAs (about  $1^\circ\text{C}$ ) first appearing over the thermocline dome region (western pole) (Fig. 8e) that cause easterly (westerly) anomalies in the second type of IOD. This is consistent with the observations.

Once the easterly (westerly) anomalies are established in the equatorial and eastern IO, the developing

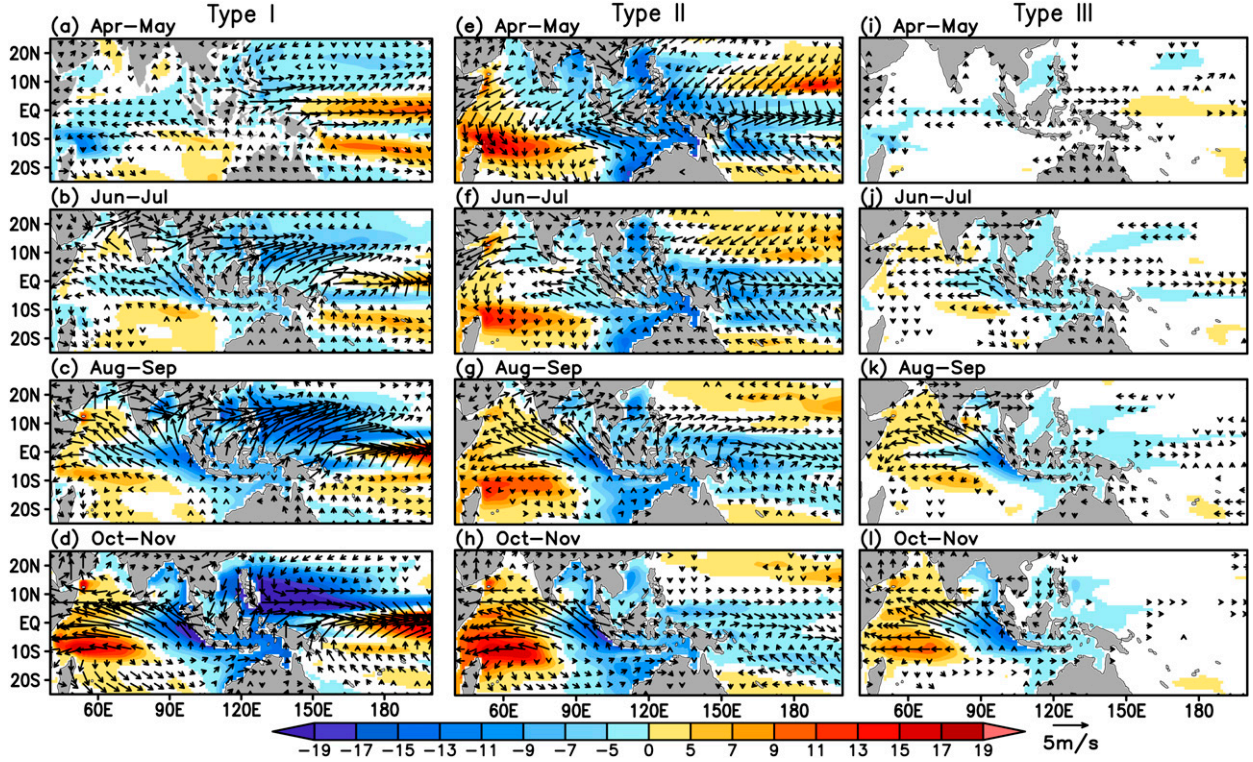


FIG. 10. As in Fig. 8, but for the SSH anomalies (shaded, cm) and SWAs (vectors,  $\text{m s}^{-1}$ ) in the PI control run in CCSM4. Shaded areas and vectors are significant at the 95% confidence level, from a Student's two-tailed *t*-test.

process from there on is similar in all three types of IODs, which depends on the local air-sea interaction in the TIO. In response to the easterly (westerly) anomalies, the equatorial thermocline in the IO elevates (deepens) to the east and deepens (elevates) to the west (Figs. 10d,h,i), thus cooling (warming) the SST in the eastern IO and warming (cooling) the SST in the western IO by the wind-thermocline-SST feedback mechanism in all three types of IODs (Figs. 8c,d, Figs. 8g,h, and Fig. 8k, respectively). When the background winds change from winter monsoon to summer monsoon in June, it is in favor of cooling (warming) along the Sumatra/Java coast and warming (cooling) along the Somalia coast due to an evaporative effect. Meanwhile, anomalous easterlies (westerlies) lead to anticyclonic (cyclonic) wind stress anomalies in the southeastern IO, which induce downwelling (upwelling) Rossby waves, propagating westward to warm (cool) the SST over the thermocline dome region (Figs. 10d,h,i). All three types of IODs form in the boreal summer and peak in the boreal fall (Fig. 8).

There are obvious differences of WC anomaly for the three types of IODs (Fig. 9). For the first type of pIOD, the usual ring motion first appears around the date line during the initial stage of the first type of IOD, which

strengthens gradually with increasing westerly (easterly) anomalies in the west equatorial Pacific (eastern equatorial IO) during the development phase (Figs. 9b,c). The strongest WC anomaly occurs in fall both in the Pacific and IO, when the IOD reaches its peak (Fig. 9d). For the second type of pIOD (Figs. 9e-h), the Indo-Pacific WC anomaly is similar to that in the first type in the boreal spring (Fig. 9e). However, both the rising branch anomaly in the central equatorial Pacific and the westerly anomalies in the western equatorial Pacific diminish gradually during the following months (Figs. 9f-h). Besides, the WC anomaly in the IO increases gradually starting in summer (June–July), and the easterly anomalies in the IO are stronger than the westerly anomalies in the Pacific during fall (Fig. 9h), which is attributed to the zonal SST gradient with significant warming in the western IO. As for the third type of pIOD (Figs. 9i-l), when the anomalous sinking and rising motions develop in the eastern and western equatorial IO respectively, there is no significant atmospheric zonal circulation anomaly in the Pacific from April–May to August–September (Figs. 9i-k). Therefore, we can conclude that the occurrence of the anomalous WC in the IO is more likely induced by the local air-sea interaction in the IO.

TABLE 3. Numbers of positive (negative) IODs of each type for the 17 CMIP5 models in the historical simulation.

CMIP5 model name	First type of IOD	Second type of IOD	Third type of IOD
CanESM2	5 (5)	3 (3)	1 (2)
CCSM4	8 (3)	6 (10)	1 (0)
CNRM-CM5	14 (12)	1 (3)	0 (0)
CSIRO-Mk3.6.0	4 (2)	7 (8)	6 (3)
GFDL-ESM2G	5 (4)	1 (4)	2 (1)
GFDL-ESM2M	10 (10)	1 (8)	1 (0)
GISS-E2-H	4 (1)	3 (3)	1 (1)
GISS-E2-R	3 (5)	0 (1)	1 (1)
HadGEM2-ES	3 (8)	6 (6)	2 (1)
INM-CM4	3 (1)	1 (4)	4 (6)
IPSL-CM5A-LR	0 (1)	5 (2)	0 (3)
IPSL-CM5A-MR	3 (4)	2 (5)	1 (0)
MIROC5	7 (6)	2 (5)	0 (3)
MPI-ESM-LR	3 (3)	2 (4)	0 (2)
MRI-CGCM3	3 (2)	2 (1)	2 (3)
NorESM1-M	9 (5)	2 (6)	1 (2)
NorESM1-ME	4 (8)	2 (0)	1 (0)

To summarize, the probabilities of the three types of IODs are 40.6%, 40.6%, and 12.2%, respectively, in the 500-yr control run, which is comparable to 46.4%, 35.7%, and 7.1% in the observations from the last 63 years. It is also encouraging that there are some similarities in the trigger conditions and evolution processes for the three types of IOD events between observations and models. The occurrences for the second and third

types of IODs are more likely induced by internal air-sea interaction within IO rather than by the remote forcing from the TP.

## 5. Three types of IODs in the historical simulations

To further verify the existence of the three types of IODs, we expanded the model from one single CCSM4

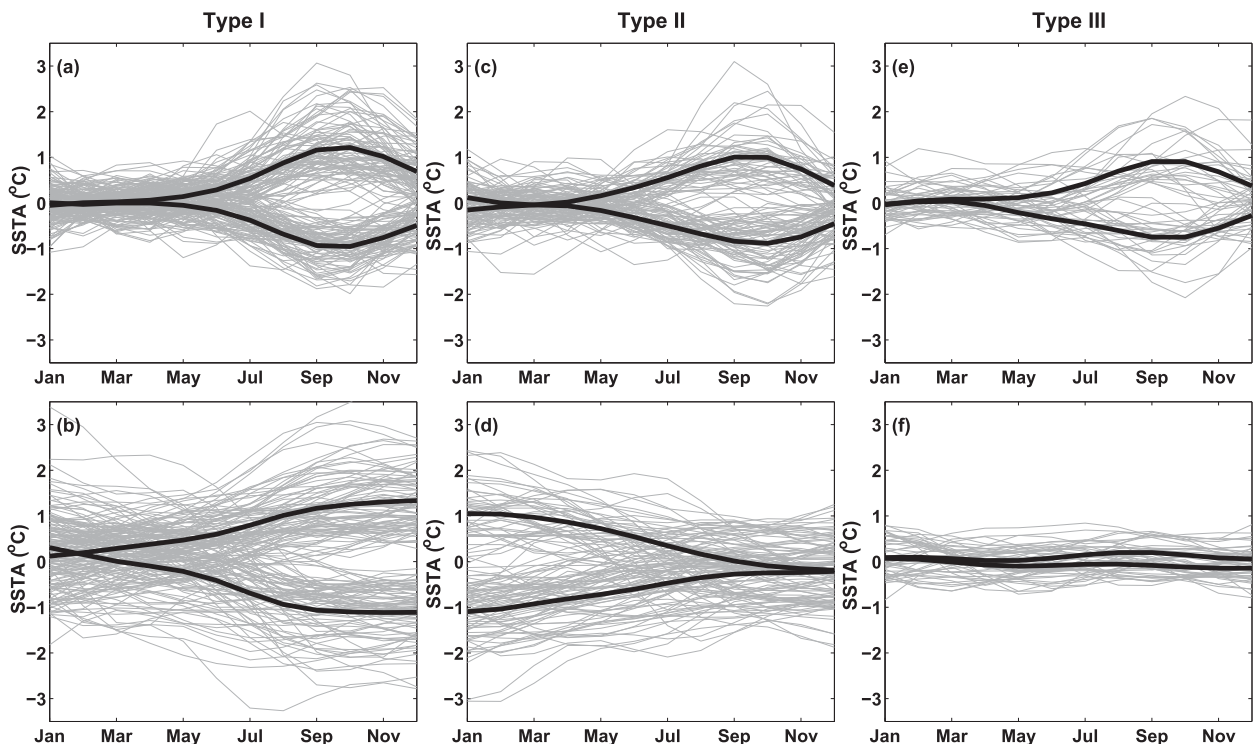


FIG. 11. As in Fig. 7, but for the historical simulation of 17 CMIP5 models.

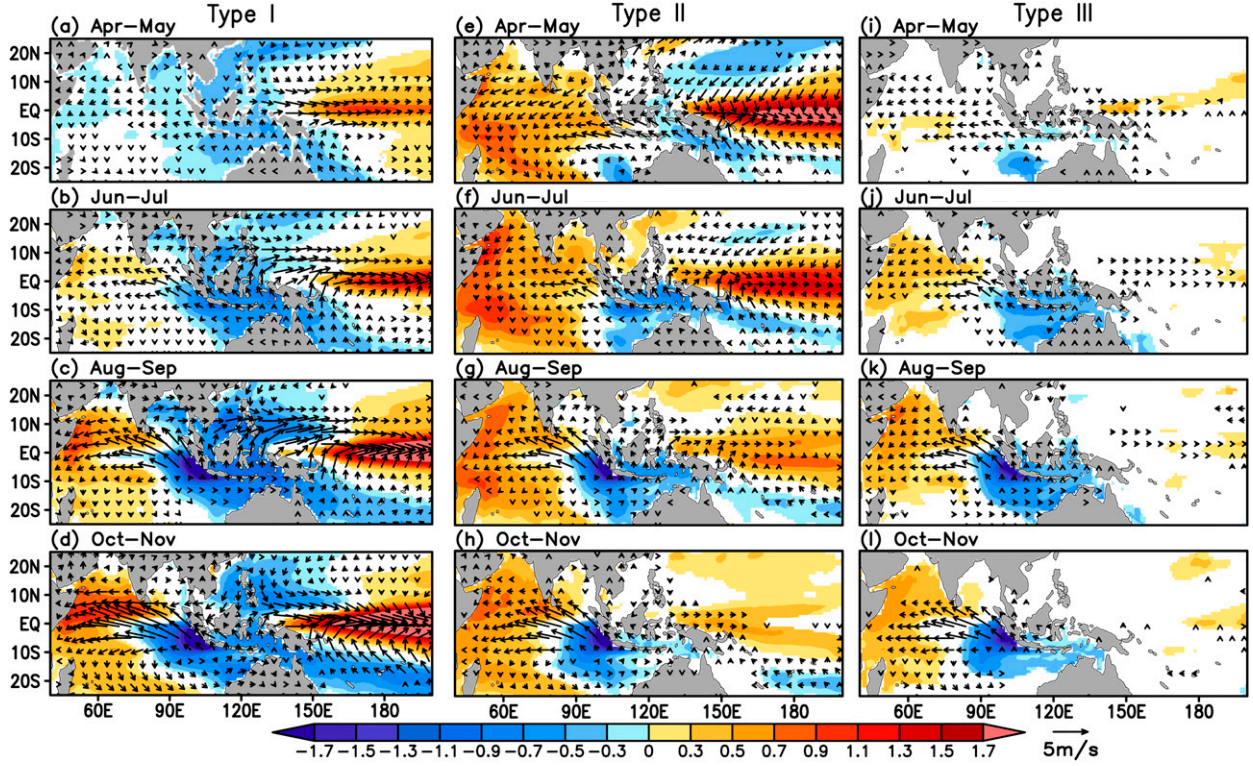


FIG. 12. As in Fig. 8, but for the historical simulation of 17 CMIP5 models.

model to 17 CMIP5 models in order to increase the sampling number of IODs and reduce the model errors. We investigated the IOD events during the 55-yr (1951–2005) historical simulations. During this period, the total numbers of the three types of IODs (nIODs) are 88 (80), 46 (73), and 24 (28), respectively, for all 17 CMIP5 models combined, as shown in Table 3. Despite differences among them, all models can simulate the first and second types of IODs, and all models except CNRM-CM5 can simulate the third type of IOD (Table 3). The probabilities of the three types of IODs in these multimodel simulations are 42.5%, 30.1%, and 13.2%, respectively, which is close to those from the observations and the PI control run. The modeled consecutive pIODs (nIODs) occur with a low frequency as in the observations and the control experiment in CCSM4. A few special IOD events from the 17 CMIP5 models described in section 3 are not considered in this study in order to keep the discussion simple and focused.

Figure 11 shows the IOD index for (top) the three types of IOD events and (bottom) their corresponding ENSO index in the multimodel historical simulations. All three types of IODs peak in the boreal fall, which is similar to the observations and the PI control run discussed earlier. The model biases show stronger ENSO and IOD simulations in the historical simulations have

little effect on the phase-locking and the classification for the three types of IODs. In the first and third types of IODs, the easterly (westerly) anomalies first occur in the equatorial and eastern IO (Figs. 12a,i) and generate local SSTAs (up to  $-0.7^{\circ}\text{C}$ ) by the wind–thermocline–SST feedback (Figs. 12b,j). Then the oceanic Rossby waves induced by SWAs affect the SST in the southwest IO when they propagate there after several months (Figs. 13d,l). In the second type of IOD, a well-defined basinwide warming (cooling) is nonuniform across the TIO in the boreal spring (Fig. 12e). The inhomogeneous warming (cooling) with significant positive (negative) SSTAs ( $0.9^{\circ}\text{C}$ ) in the western IO by June–July (Fig. 12f) results from downwelling (upwelling) Rossby waves and WES feedback. Thus, easterly (westerly) anomalies converge (diverge) westward due to the anomalous zonal SST gradient from boreal spring to fall. By late summer, the basinwide warm (cold) SSTAs are replaced by cold (warm) SSTAs in the eastern IO through the wind–thermocline–SST feedback. Then the basinwide warming (cooling) gives way to the IOD in the TIO in August–September (Fig. 12g). These processes shown here are in good agreement with those in the observations and the control run in Figs. 4, 5, 8, and 10.

Previous studies have shown that the relation of IOD with ENSO has been stronger since the mid-1970s (e.g.,

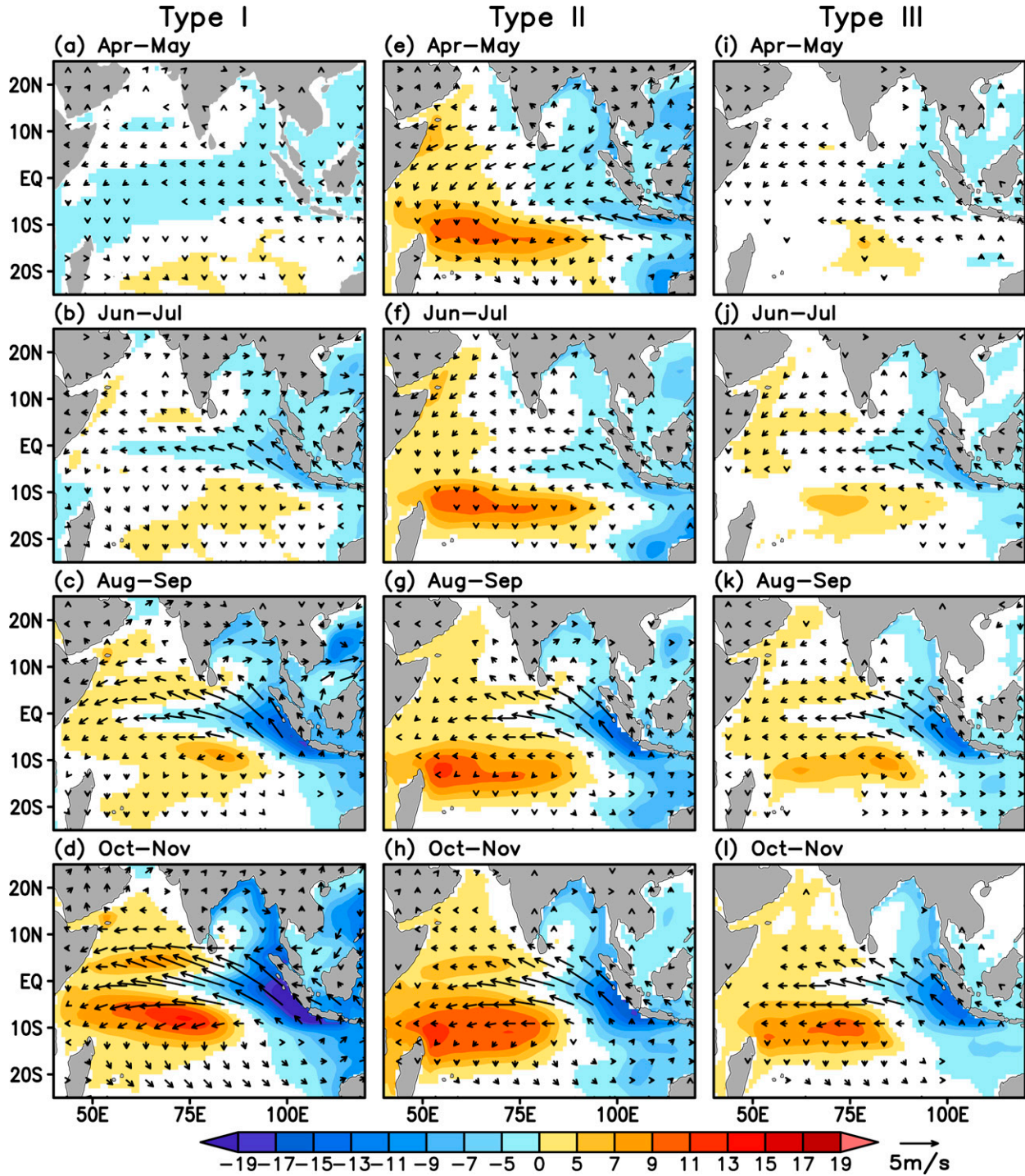


FIG. 13. As in Fig. 10, but for the historical simulation of 17 CMIP5 models.

Xie et al. 2010; Du et al. 2013a). However, we do not find this trend in the historical multimodel results of 1976–2005. The probabilities of the three types of IODs during this period are 42%, 32.1%, and 13%, respectively, which is largely unchanged after 1976.

## 6. Conclusions and discussion

Based on the observational data, model simulations from the PI control run of CCSM4 and the historical simulations in the 17 CMIP5 models, we categorize IODs

with a peak in the fall into three types according to different trigger conditions. These are 1) pIODs (nIODs) occurring in the developing phase of El Niño (La Niña); 2) pIODs (nIODs) appearing in the year after El Niño (La Niña), which are transformed from inhomogeneous basinwide warming (cooling) in the TIO; and 3) IODs without any relation with ENSO. The probabilities of the three types of IODs are 40.6%, 40.6%, and 12.2% respectively in the 500-yr control run and 42.5%, 30.1%, and 13.2% respectively in the 1951–2005 historical simulation. Both probabilities are comparable with estimates from the past 63-yr observational period (46.4%, 35.7%, and 7.1%). Although most models simulate stronger intensity of ENSO and IOD than the observations, this has little effect on the phase-locking and the classification of the IOD. Furthermore, the trigger conditions and formation mechanisms for the three types of IODs in the control run and the CMIP5 multimodel ensemble are similar to the observations, adding confidence in the IOD simulations in the CCSM4 model and the 17 CMIP5 models used in this study.

Among the three types of IODs, the trigger conditions are different. The first type of IOD starts with easterly (westerly) anomalies in the eastern IO resulting from the weakened (strengthened) Indo-Pacific WC caused by the El Niño (La Niña) in the Pacific. In the third type, the pure IOD, the easterly (westerly) anomalies come from a strengthened (weakened) cross-equatorial flow such as the Asia–Australia summer monsoon in June–July. The trigger conditions for these two types are consistent with previous studies mentioned earlier. We identify the second type of IOD, where the easterly (westerly) anomalies are triggered by an anomalous zonal SST gradient in the year following El Niño (La Niña). The westward-propagating Rossby waves and WES feedback mechanisms lead to the zonal SST gradient, which are considered to be crucial during the early development in the second type. The occurrences of the second and third type of IODs are more likely induced by the internal air–sea interaction within IO rather than by remote forcing from the TP.

Once the easterly (westerly) anomalies appear in the eastern TIO, the developing processes are similar in all three types of IODs. Cold (warm) SSTAs in the eastern TIO occur in the boreal summer and gradually strengthen by the wind–thermocline–SST feedback afterward. Furthermore, when the summer monsoon onset occurs in June, the SWAs help cool (warm) the SST along the Sumatra/Java coast and warm (cool) the SST along the Somalia coast due to evaporative effects. Besides, the downwelling (upwelling) Rossby waves induced by SWAs propagate westward and impact the SST over the thermocline dome region in the boreal fall.

All three types of IODs reach their peak in the boreal fall.

Here we present a broad approach to defining IOD types based on their relation with ENSO. We find that the models are useful in providing detailed information on IOD trigger conditions and mechanisms. Nevertheless, there are still considerable uncertainties in the CMIP5 models due to the model biases described in section 2, which set limits to our study in the real climate. However, these model biases have little effect on the classification of the three types of IOD, and the coupled climate models are able to simulate the three types of IODs with trigger conditions and probabilities similar to those in the observations, where the three types of IOD events do exist, including the second type of IOD transformed from inhomogeneous basinwide warming or cooling.

**Acknowledgments.** We thank Dr. Xiaotong Zheng and three anonymous reviewers for their constructive comments and suggestions. This work is supported by the National Basic Research Program of China 2012CB955603, Natural Science Foundation of China (41176006 and 41221063), China Meteorological Public Welfare Scientific Research Project (GYHY201306027), and Shandong Joint Fund for Marine Science Research Centers (U1406401). Much of the work was performed when Feiyan Guo was a visiting student at the National Oceanic and Atmospheric Administration and is supported by the China Scholarship Council. We thank the climate modeling groups (listed in Table 1) for producing and making their model outputs available. We acknowledge the World Climate Research Programme’s Working Group on Coupled Modelling. The U.S. Department of Energy’s Program for Climate Model Diagnosis and Intercomparison provided coordinating support and led development of software infrastructure in partnership with the Global Organization for Earth System Science Portals. John Osborn helped with technical editing.

## REFERENCES

Alexander, M. A., I. Bladé, M. Newman, J. R. Lanzante, N. C. Lau, and J. D. Scott, 2002: The atmospheric bridge: The influence of ENSO teleconnections on air–sea interaction over the global oceans. *J. Climate*, **15**, 2205–2231, doi:10.1175/1520-0442(2002)015<2205: TABTIO>2.0.CO;2.

Allan, R. J., and Coauthors, 2001: Is there an Indian Ocean dipole, and is it independent of the El Niño–Southern Oscillation? *CLIVAR Exchanges*, No. 6, International CLIVAR Project Office, Southampton, United Kingdom, 18–22.

Anderson, D., 1999: Extremes in the Indian Ocean. *Nature*, **401**, 337–339, doi:10.1038/43807.

Annamalai, H., R. Murtugudde, J. Potemra, S. P. Xie, P. Liu, and B. Wang, 2003: Coupled dynamics over the Indian Ocean:

Spring initiation of the zonal mode. *Deep-Sea Res.*, **50B**, 2305–2330, doi:[10.1016/s0967-0645\(03\)00058-4](https://doi.org/10.1016/s0967-0645(03)00058-4).

Ashok, K., Z. Guan, and T. Yamagata, 2001: Impact of the Indian Ocean dipole on the relationship between the Indian monsoon rainfall and ENSO. *Geophys. Res. Lett.*, **28**, 4499–4502, doi:[10.1029/2001GL013294](https://doi.org/10.1029/2001GL013294).

—, —, and —, 2003: A look at the relationship between the ENSO and the Indian Ocean dipole. *J. Meteor. Soc. Japan*, **81**, 41–56, doi:[10.2151/jmsj.81.41](https://doi.org/10.2151/jmsj.81.41).

Behera, S. K., R. Krishnan, and T. Yamagata, 1999: Unusual ocean–atmosphere conditions in the tropical Indian Ocean during 1994. *Geophys. Res. Lett.*, **26**, 3001–3004, doi:[10.1029/1999GL010434](https://doi.org/10.1029/1999GL010434).

—, J.-J. Luo, S. Masson, P. Delecluse, S. Gualdi, A. Navarra, and T. Yamagata, 2005: Paramount impact of the Indian Ocean dipole on the East African short rains: A CGCM study. *J. Climate*, **18**, 4514–4530, doi:[10.1175/JCLI3541.1](https://doi.org/10.1175/JCLI3541.1).

—, —, —, S. A. Rao, H. Sakuma, and T. Yamagata, 2006: A CGCM study on the interaction between IOD and ENSO. *J. Climate*, **19**, 1688–1705, doi:[10.1175/JCLI3797.1](https://doi.org/10.1175/JCLI3797.1).

—, —, and T. Yamagata, 2008: Unusual IOD event of 2007. *Geophys. Res. Lett.*, **35**, L14S11, doi:[10.1029/2008GL034122](https://doi.org/10.1029/2008GL034122).

Bellenger, H., E. Guilyardi, J. Leloup, M. Lengaigne, and J. Vialard, 2014: ENSO representation in climate models: From CMIP3 to CMIP5. *Climate Dyn.*, **42**, 1999–2018, doi:[10.1007/s00382-013-1783-z](https://doi.org/10.1007/s00382-013-1783-z).

Black, E., J. Slingo, and K. R. Sperber, 2003: An observational study of the relationship between excessively strong short rains in coastal East Africa and Indian Ocean SST. *Mon. Wea. Rev.*, **131**, 74–94, doi:[10.1175/1520-0493\(2003\)131<0074:AOSOTR>2.0.CO;2](https://doi.org/10.1175/1520-0493(2003)131<0074:AOSOTR>2.0.CO;2).

Bracco, A., F. Kucharski, F. Molteni, W. Hazeleger, and C. Severijns, 2005: Internal and forced modes of variability in the Indian Ocean. *Geophys. Res. Lett.*, **32**, L12707, doi:[10.1029/2005GL023154](https://doi.org/10.1029/2005GL023154).

Bradley, R. S., H. F. Diaz, G. N. Kiladis, and J. K. Eischeid, 1987: ENSO signal in continental temperature and precipitation records. *Nature*, **327**, 497–501, doi:[10.1038/327497a0](https://doi.org/10.1038/327497a0).

Cai, W., and T. Cowan, 2013: Why is the amplitude of the Indian Ocean dipole overly large in CMIP3 and CMIP5 climate models? *Geophys. Res. Lett.*, **40**, 1200–1205, doi:[10.1002/grl.50208](https://doi.org/10.1002/grl.50208).

—, —, and M. Raupach, 2009a: Positive Indian Ocean dipole events precondition southeast Australia bushfires. *Geophys. Res. Lett.*, **36**, L19710, doi:[10.1029/2009GL039902](https://doi.org/10.1029/2009GL039902).

—, —, and A. Sullivan, 2009b: Recent unprecedented skewness towards positive Indian Ocean dipole occurrences and its impact on Australian rainfall. *Geophys. Res. Lett.*, **36**, L11705, doi:[10.1029/2009GL037604](https://doi.org/10.1029/2009GL037604).

—, P. van Rensch, T. Cowan, and H. H. Hendon, 2011: Teleconnection pathways of ENSO and the IOD and the mechanisms for impacts on Australian rainfall. *J. Climate*, **24**, 3910–3923, doi:[10.1175/2011JCLI4129.1](https://doi.org/10.1175/2011JCLI4129.1).

—, —, —, and —, 2012: An asymmetry in the IOD and ENSO teleconnection pathway and its impact on Australian climate. *J. Climate*, **25**, 6318–6329, doi:[10.1175/JCLI-D-11-00501.1](https://doi.org/10.1175/JCLI-D-11-00501.1).

—, X.-T. Zheng, E. Weller, M. Collins, T. Cowan, M. Lengaigne, W. D. Yu, and T. Yamagata, 2013: Projected response of the Indian Ocean Dipole to greenhouse warming. *Nat. Geosci.*, **6**, 999–1007, doi:[10.1038/ngeo2009](https://doi.org/10.1038/ngeo2009).

Carton, J. A., and B. S. Giese, 2008: A reanalysis of ocean climate using Simple Ocean Data Assimilation (SODA). *Mon. Wea. Rev.*, **136**, 2999–3017, doi:[10.1175/2007MWR1978.1](https://doi.org/10.1175/2007MWR1978.1).

Chowdary, J. S., and C. Gnanaseelan, 2007: Basinwide warming of the Indian Ocean during El Niño and Indian Ocean dipole years. *Int. J. Climatol.*, **27**, 1421–1428, doi:[10.1002/joc.1482](https://doi.org/10.1002/joc.1482).

Deser, C., and Coauthors, 2012: ENSO and Pacific decadal variability in the Community Climate System Model version 4. *J. Climate*, **25**, 2622–2651, doi:[10.1175/JCLI-D-11-00301.1](https://doi.org/10.1175/JCLI-D-11-00301.1).

Drrohblav, H.-K. L., S. Gualdi, and A. Navarra, 2007: A diagnostic study of the Indian Ocean dipole mode in El Niño and non–El Niño years. *J. Climate*, **20**, 2961–2977, doi:[10.1175/JCLI4153.1](https://doi.org/10.1175/JCLI4153.1).

Du, Y., S.-P. Xie, G. Huang, and K.-M. Hu, 2009: Role of air–sea interaction in the long persistence of El Niño–induced north Indian Ocean warming. *J. Climate*, **22**, 2023–2038, doi:[10.1175/2008JCLI2590.1](https://doi.org/10.1175/2008JCLI2590.1).

—, W. Cai, and Y. Wu, 2013a: A new type of the Indian Ocean dipole since the mid-1970s. *J. Climate*, **26**, 959–972, doi:[10.1175/JCLI-D-12-00047.1](https://doi.org/10.1175/JCLI-D-12-00047.1).

—, S.-P. Xie, Y.-L. Yang, X.-T. Zheng, L. Liu, and G. Huang, 2013b: Indian Ocean variability in the CMIP5 multimodel ensemble: The basin mode. *J. Climate*, **26**, 7240–7266, doi:[10.1175/JCLI-D-12-00678.1](https://doi.org/10.1175/JCLI-D-12-00678.1).

Fasullo, J. T., C. Boening, F. W. Landerer, and R. S. Nerem, 2013: Australia’s unique influence on global sea level in 2010–2011. *Geophys. Res. Lett.*, **40**, 4368–4373, doi:[10.1002/grl.50834](https://doi.org/10.1002/grl.50834).

Fischer, A., P. Terray, E. Guilyardi, S. Gualdi, and P. Delecluse, 2005: Two independent triggers for the Indian Ocean dipole/zonal mode in a coupled GCM. *J. Climate*, **18**, 3428–3449, doi:[10.1175/JCLI3478.1](https://doi.org/10.1175/JCLI3478.1).

Gualdi, S., E. Guilyardi, A. Navarra, S. Masina, and P. Delecluse, 2003: The interannual variability in the tropical Indian Ocean as simulated by a CGCM. *Climate Dyn.*, **20**, 567–582.

Guilyardi, E., and Coauthors, 2012: A first look at ENSO in CMIP5. *CLIVAR Exchanges*, No. 17, International CLIVAR Project Office, Southampton, United Kingdom, 29–32.

Guo, F., Q. Liu, X.-T. Zheng, and S. Sun, 2013: The role of barrier layer in southeastern Arabian Sea during the development of positive Indian Ocean Dipole events. *J. Ocean Univ. China*, **12**, 245–252, doi:[10.1007/s11802-013-2170-4](https://doi.org/10.1007/s11802-013-2170-4).

Hong, C.-C., M.-M. Lu, and M. Kanamitsu, 2008a: Temporal and spatial characteristics of positive and negative Indian Ocean dipole with and without ENSO. *J. Geophys. Res.*, **113**, D08107, doi:[10.1029/2007JD009151](https://doi.org/10.1029/2007JD009151).

—, T. Li, and J.-J. Luo, 2008b: Asymmetry of the Indian Ocean dipole. Part II: Model diagnosis. *J. Climate*, **21**, 4849–4858, doi:[10.1175/2008JCLI2223.1](https://doi.org/10.1175/2008JCLI2223.1).

—, —, LinHo, and Y.-C. Chen, 2010: Asymmetry of the Indian Ocean basinwide SST anomalies: Roles of ENSO and IOD. *J. Climate*, **23**, 3563–3576, doi:[10.1175/2010JCLI3320.1](https://doi.org/10.1175/2010JCLI3320.1).

Hong, X., H. Hu, X. Yang, Y. Zhang, G. Liu, and W. Liu, 2014: Influences of Indian Ocean interannual variability on different stages of El Niño: A FOAM1.5 model approach. *Sci. China: Earth Sci.*, **57**, 2616–2627, doi:[10.1007/s11430-014-4932-2](https://doi.org/10.1007/s11430-014-4932-2).

Huang, B., and J. L. Kinter III, 2002: Interannual variability in the tropical Indian Ocean. *J. Geophys. Res.*, **107**, 3199, doi:[10.1029/2001JC001278](https://doi.org/10.1029/2001JC001278).

Izumo, T., and Coauthors, 2010: Influence of the state of the Indian Ocean Dipole on the following year’s El Niño. *Nat. Geosci.*, **3**, 168–172, doi:[10.1038/ngeo760](https://doi.org/10.1038/ngeo760).

Kalnay, E., and Coauthors, 1996: The NCEP/NCAR 40-Year Reanalysis Project. *Bull. Amer. Meteor. Soc.*, **77**, 437–471, doi:[10.1175/1520-0477\(1996\)077<0437:TNYRP>2.0.CO;2](https://doi.org/10.1175/1520-0477(1996)077<0437:TNYRP>2.0.CO;2).

Kim, S. T., and J.-Y. Yu, 2012: The two types of ENSO in CMIP5 models. *Geophys. Res. Lett.*, **39**, L11704, doi:[10.1029/2012GL052006](https://doi.org/10.1029/2012GL052006).

Klein, S. A., B. J. Soden, and N.-C. Lau, 1999: Remote sea surface temperature variations during ENSO: Evidence for a tropical atmospheric bridge. *J. Climate*, **12**, 917–932, doi:10.1175/1520-0442(1999)012<0917:RSSTVD>2.0.CO;2.

Lau, N.-C., and M. J. Nath, 2003: Atmosphere–ocean variations in the Indo-Pacific Sector during ENSO episodes. *J. Climate*, **16**, 3–20, doi:10.1175/1520-0442(2003)016<0003:AOVITI>2.0.CO;2.

Li, G., and S.-P. Xie, 2014: Tropical biases in CMIP5 multimodel ensemble: The excessive equatorial Pacific cold tongue and double ITCZ problems. *J. Climate*, **27**, 1765–1780, doi:10.1175/JCLI-D-13-00337.1.

—, —, and Y. Du, 2015: Monsoon-induced biases of climate models over the tropical Indian Ocean. *J. Climate*, **28**, 3508–3072, doi:10.1175/JCLI-D-14-00740.1.

Li, T., B. Wang, C.-P. Chang, and Y. Zang, 2003: A theory for the Indian Ocean dipole-zonal mode. *J. Atmos. Sci.*, **60**, 2119–2135, doi:10.1175/1520-0469(2003)060<2119:ATFTIO>2.0.CO;2.

Liu, L., S.-P. Xie, X.-T. Zheng, T. Li, Y. Du, G. Huang, and W.-D. Yu, 2014: Indian Ocean variability in the CMIP5 multi-model ensemble: The zonal dipole mode. *Climate Dyn.*, **43**, 1715–1730, doi:10.1007/s00382-013-2000-9.

Liu, Q., F. Guo, and X.-T. Zheng, 2013: Relationships of interannual variability between the equatorial Pacific and tropical Indian Ocean in 17 CMIP5 models. *J. Ocean Univ. China*, **12**, 237–244, doi:10.1007/s11802-013-2195-8.

Loschnigg, J., G. Meehl, P. Webster, J. Arblaster, and G. Compo, 2003: The Asian monsoon, the tropical biennial oscillation, and the Indian Ocean zonal mode in the NCAR CSM. *J. Climate*, **16**, 1617–1642, doi:10.1175/1520-0442(2003)016<1617:TAMTTB>2.0.CO;2.

Meehl, G. A., J. M. Arblaster, and J. Loschnigg, 2003: Coupled ocean–atmosphere dynamical processes in the tropical Indian and Pacific Oceans and the TBO. *J. Climate*, **16**, 2138–2158, doi:10.1175/2767.1.

Meyers, G. A., P. C. McIntosh, L. Pigot, and M. J. Pook, 2007: The years of El Niño, La Niña, and interactions with the tropical Indian Ocean. *J. Climate*, **20**, 2872–2880, doi:10.1175/JCLI4152.1.

Murtugudde, R., J. P. McCreary Jr., and A. J. Busalacchi, 2000: Oceanic processes associated with anomalous events in the Indian Ocean with relevance to 1997–98. *J. Geophys. Res.*, **105**, 3295–3306, doi:10.1029/1999JC900294.

Philander, S. G. H., 1990: *El Niño, La Niña, and the Southern Oscillation*. Academic Press, 293 pp.

Privalsky, V. E., and D. T. Jensen, 1995: Assessment of the influence of ENSO on annual global air temperatures. *Dyn. Atmos. Oceans*, **22**, 161–178, doi:10.1016/0377-0265(94)00400-Q.

Rao, J., and R.-C. Ren, 2014: Statistical characteristics of ENSO events in CMIP5 models. *Atmos. Oceanic Sci. Lett.*, **7**, 546–552, doi:10.3878/AOSL20140055.

Rao, S. A., and S. K. Behera, 2005: Subsurface influence on SST in the tropical Indian Ocean: Structure and interannual variability. *Dyn. Atmos. Oceans*, **39**, 103–135, doi:10.1016/j.dynatmoce.2004.10.014.

—, —, Y. Masumoto, and T. Yamagata, 2002: Interannual variability in the subsurface tropical Indian Ocean with a special emphasis on the Indian Ocean Dipole. *Deep-Sea Res. II*, **49**, 1549–1572, doi:10.1016/S0967-0645(01)00158-8.

Rasmusson, E. M., and T. H. Carpenter, 1982: Variations in tropical sea surface temperature and surface wind fields associated with the Southern Oscillation/El Niño. *Mon. Wea. Rev.*, **110**, 354–384, doi:10.1175/1520-0493(1982)110<0354:VITSST>2.0.CO;2.

Saji, N. H., and T. Yamagata, 2003: Structure of SST and surface wind variability during Indian Ocean dipole mode events: COADS observations. *J. Climate*, **16**, 2735–2751, doi:10.1175/1520-0442(2003)016<2735:SOSASW>2.0.CO;2.

—, B. N. Goswami, P. N. Vinayachandran, and T. Yamagata, 1999: A dipole mode in the tropical Indian Ocean. *Nature*, **401**, 360–363.

—, S.-P. Xie, and T. Yamagata, 2006: Tropical Indian Ocean variability in the IPCC twentieth-century climate simulations. *J. Climate*, **19**, 4397–4417, doi:10.1175/JCLI3847.1.

Schott, F. A., S.-P. Xie, and J. P. McCreary, 2009: Indian Ocean circulation and climate variability. *Rev. Geophys.*, **47**, RG1002, doi:10.1029/2007RG000245.

Shinoda, T., M. A. Alexander, and H. H. Hendon, 2004a: Remote response of the Indian Ocean to interannual SST variations in the tropical Pacific. *J. Climate*, **17**, 362–372, doi:10.1175/1520-0442(2004)017<0362:RROTIO>2.0.CO;2.

—, H. H. Hendon, and M. A. Alexander, 2004b: Surface and subsurface dipole variability in the Indian Ocean and its relation with ENSO. *Deep-Sea Res. I*, **51**, 619–635, doi:10.1016/j.dsr.2004.01.005.

Smith, T. M., R. W. Reynolds, T. C. Peterson, and J. Lawrimore, 2008: Improvements to NOAA’s historical merged land–ocean surface temperature analysis (1880–2006). *J. Climate*, **21**, 2283–2296, doi:10.1175/2007JCLI2100.1.

Spencer, H., R. T. Sutton, J. M. Slingo, M. Roberts, and E. Black, 2005: Indian Ocean climate and dipole variability in Hadley Centre coupled GCMs. *J. Climate*, **18**, 2286–2307, doi:10.1175/JCLI3410.1.

Taschetto, A. S., A. Sen Gupta, N. Jourdain, A. Santoso, C. C. Ummenhofer, and M. H. England, 2014: Cold tongue and warm pool ENSO events in CMIP5: Mean state and future projections. *J. Climate*, **27**, 2861–2885, doi:10.1175/JCLI-D-13-00437.1.

Taylor, K. E., R. J. Stouffer, and G. A. Meehl, 2012: An overview of CMIP5 and the experiment design. *Bull. Amer. Meteor. Soc.*, **93**, 485–498, doi:10.1175/BAMS-D-11-00094.1.

Terray, P., F. Chauvin, and H. Douville, 2007: Impact of southeast Indian Ocean sea surface temperature anomalies on monsoon–ENSO–dipole variability in a coupled ocean–atmosphere model. *Climate Dyn.*, **28**, 553–580, doi:10.1007/s00382-006-0192-y.

Trenberth, K. E., G. W. Branstator, D. Karoly, A. Kumar, N.-C. Lau, and C. Ropelewski, 1998: Progress during TOGA in understanding and modeling global teleconnections associated with tropical sea surface temperatures. *J. Geophys. Res.*, **103**, 14 291–14 324, doi:10.1029/97JC01444.

Vinayachandran, P. N., N. H. Saji, and T. Yamagata, 1999: Response of the equatorial Indian Ocean to an anomalous wind event during 1994. *Geophys. Res. Lett.*, **26**, 1613–1616, doi:10.1029/1999GL900179.

Webster, P. J., A. M. Moore, J. P. Loschnigg, and R. R. Leben, 1999: Coupled ocean–atmosphere dynamics in the Indian Ocean during 1997–98. *Nature*, **401**, 356–360, doi:10.1038/43848.

Wu, R., B. P. Kirtman, and V. Krishnamurthy, 2008: An asymmetric mode of tropical Indian Ocean rainfall variability in boreal spring. *J. Geophys. Res.*, **113**, D05104, doi:10.1029/2007JD009316.

Xie, S.-P., and S. G. H. Philander, 1994: A coupled ocean–atmosphere model of relevance to the ITCZ in the eastern Pacific. *Tellus*, **46A**, 340–350, doi:10.1034/j.1600-0870.1994.t01-1-00001.x.

—, H. Annamalai, F. A. Schott, and J. P. McCreary, 2002: Structure and mechanisms of south Indian Ocean climate variability.

*J. Climate*, **15**, 864–878, doi:10.1175/1520-0442(2002)015<0864: SAMOSI>2.0.CO;2.

—, Y. Du, G. Huang, X.-T. Zheng, H. Tokinaga, K. Hu, and Q. Liu, 2010: Decadal shift in El Niño influences on Indo-western Pacific and East Asian climate in the 1970s. *J. Climate*, **23**, 3352–3368, doi:10.1175/2010JCLI3429.1.

Yamagata, T., S. K. Behera, S. A. Rao, Z. Guan, K. Ashok, and H. N. Saji, 2003: Comments on “Dipoles, temperature gradient, and tropical climate anomalies.” *Bull. Amer. Meteor. Soc.*, **84**, 1418–1422, doi:10.1175/BAMS-84-10-1418.

—, —, J.-J. Luo, S. Masson, M. Jury, and S. A. Rao, 2004: Coupled ocean–atmosphere variability in the tropical Indian Ocean. *Earth Climate: The Ocean–Atmosphere Interaction, Geophys. Monogr.*, Vol. 147, Amer. Geophys. Union, 189–212.

Yang, J., Q. Liu, S.-P. Xie, Z. Liu, and L. Wu, 2007: Impact of the Indian Ocean SST basin mode on the Asian summer monsoon. *Geophys. Res. Lett.*, **34**, L02708, doi:10.1029/2006GL028571.

—, —, and Z. Liu, 2010: Linking observations of the Asian monsoon to the Indian Ocean SST: Possible roles of Indian Ocean basin mode and dipole mode. *J. Climate*, **23**, 5889–5902, doi:10.1175/2010JCLI2962.1.

Yu, L., 2003: Variability of the depth of the 20°C isotherm along 6°N in the Bay of Bengal: Its response to remote and local forcing and its relation to satellite SSH variability. *Deep-Sea Res. II*, **50**, 2285–2304, doi:10.1016/S0967-0645(03)00057-2.

—, —, and M. M. Rienecker, 2000: Indian Ocean warming of 1997–1998. *J. Geophys. Res.*, **105**, 16 923–16 939, doi:10.1029/2000JC900068.

Zheng, X.-T., S.-P. Xie, G. A. Vecchi, Q. Liu, and J. Hafner, 2010: Indian Ocean dipole response to global warming: Analysis of ocean–atmospheric feedbacks in a coupled model. *J. Climate*, **23**, 1240–1253, doi:10.1175/2009JCLI3326.1.

—, —, Y. Du, L. Liu, G. Huang, and Q. Liu, 2013: Indian Ocean dipole response to global warming in the CMIP5 multimodel ensemble. *J. Climate*, **26**, 6067–6080, doi:10.1175/JCLI-D-12-00638.1.

Zhong, A., H. H. Hendon, and O. Alves, 2005: Indian Ocean variability and its association with ENSO in a global coupled model. *J. Climate*, **18**, 3634–3649, doi:10.1175/JCLI3493.1.

Zhou, Z.-Q., S.-P. Xie, X.-T. Zheng, Q. Liu, and H. Wang, 2014: Global warming–induced changes in El Niño teleconnections over the North Pacific and North America. *J. Climate*, **27**, 9050–9064, doi:10.1175/JCLI-D-14-00254.1.